GEPP-308

DIELECTRIC CHARACTERISTICS OF PZT 95/5 FERROELECTRIC CERAMICS AT HIGH PRESSURES

R. K. Spears
Laboratory Operation

January 31, 1978

General Electric Company
Neutron Devices Department
P. O. Box 11508
St. Petersburg, Florida 33733

Prepared for the U. S.
Department of Energy
Albuquerque Operations Office
Under Contract No. EY-76-C-04-0656

ABSTRACT

The room temperature dielectric properties of a ferroelectric ceramic having a nominal composition of 95 atomic percent lead zirconate and 5 atomic percent lead titanate (designated as PZT 95/5) with a niobium dopant was examined at high hydrostatic pressures using a tetrahedral anvil apparatus. This ceramic has practical applications as a power source in which large quantities of charge are released by dynamic (shock wave) depolarization. Numerous mathematical models of this process have been proposed; however, the use of models has been limited because of the lack of high pressure electrical properties. This study attempted to provide these data on PZT 95/5 by determining the small signal and high electric field dielectric properties at pressures over 4 GPa.

A stainless steel test cell was fabricated which contained a Manganin* pressure sensing gage, the sample, and the insulating fluid (1-to-1 mixture of isopentane and n-pentane). Polyethylene plugs held the fluid in place and one plug having containing holes No. 28 magnet lead wire which was capable of supplying 2000 volts to the specimen.

Pressure depolarization of PZT 95/5 is attributed to the inducement of the 0.4 GPa nonpolar antiferroelectric phase; thus, the bound ferroelectric charge is released at the transition. Experimental shock propagation studies on PZT 95/5 have resulted in a two-, and sometimes three-wave structure. There has been some indication of additional high pressure phases. An additional objective was to detect high pressure phase changes using dielectric measurements.

When the dielectric constant was plotted versus pressure, there was a gradual increase up to the ferroelectric-antiferroelectric transition. The dielectric constant then fell and gradually leveled off. At approximately 2 GPa, a dielectric anomaly was observed on every test. This was initially attributed to a phase change; however, due to the fact that it was irreversible and that the sample after this anomaly was extremely fragile, the cause was attributed to the collapse of pores in the ceramic.

---

*Trademark, Wilbur B. Driver Co.

Hysteresis loops were run on specimens up to the transition. It was found that the antiferroelectric state could be induced at a lower pressure than had been measured using small signal techniques by continued looping at an intermediate pressure. This value is probably a truer transition than that determined by small signal measurements. The latter is apparently a measurement made while the sample is in a metastable ferroelectric state.

When a sample was retested at zero psi after it had been pressure depolarized, only 180° domain realignment was evident as opposed to 180° and 90° on thermally depoled samples. This as well as other dielectric data indicate that the metastable antiferroelectric phase may be retained to zero pressure (in the absence of an electric field).

As with other ferroelectric materials (like $BaTiO_3$), it was possible to fit small signal data at pressures immediately greater than the ferroelectric-antiferroelectric transition in the antiferroelectric state to a Curie-Weiss-like relationship, $\varepsilon = C^*/(p-p_o)$. However, a two-termed rather than a one-termed equation was needed. The second term consisted of the y intercept.

These results could be applied directly to some of the simplified shock depolarization models. However, current theories make use of the electric relaxation characteristics of dielectrics. An examination consisting of plotting the complex dielectric modulus components revealed that to use these data effectively, measurements at higher frequencies would be required.

CONTENTS

Section	Page
INTRODUCTION	1
BACKGROUND	3
Properties of Dielectrics	3
Ferroelectricity	6
Ferroelectric Composition PZT 95/5	12
Ferroelectrics at High Pressure	16
High Pressure Static Test Apparatus	19
EXPERIMENTAL PROGRAM	21
Tetrahedral Anvil Apparatus	21
Test Cell	24
Instrumentation and Measurement Technique	24
Test Procedure	27
Data Analysis	28
RESULTS	30
Overall Results	30
Low Pressure Dielectric Characteristics	36
Curie-Weiss-Like Behavior	40
Frequency Dependent Behavior	43
SUMMARY AND CONCLUSIONS	47
APPENDIX A - TETRAHEDRAL PRESS DESCRIPTION AND OPERATION	49
APPENDIX B - FABRICATION OF TETRAHEDRON	55
APPENDIX C - CONSTRUCTION OF THE MANGANIN CELL	58
APPENDIX D - FERROELECTRIC SAMPLES	62
APPENDIX E - FABRICATION OF CAPSULE, PLUGS AND LEAD WIRES	63
APPENDIX F - DIELECTRIC TEST FLUID	67
APPENDIX G - ASSEMBLY OF CAPSULE AND TEST CELL	68
APPENDIX H - CALIBRATION OF THE MANGANIN GAGE AND HEISE GAGE	71
ACKNOWLEDGMENTS	76
REFERENCES	77

ILLUSTRATIONS

Figure		Page
1	Typical Polarization Versus Electric Field Hysteresis Loop for Ferroelectric Materials	8
2	Polarization Versus Electric Field for an Antiferroelectric Material With Field Enforced Ferroelectricity	11
3	Electric Field Versus Temperature Showing Phases Encountered for Some Ferroelectric Materials When Looped at T_1 and T_2	12
4	Temperature Versus Composition Phase Diagram for Lead Zirconate-Lead Titanate (No Niobium)	13
5	Ternary Compositional Phase Diagram at Room Temperature for $PbZrO_3$, $PbTiO_2$, and $PbNb_2O_6$ Near the 100% $PbZrO_3$ Composition	15
6	Temperature Compositional Phase Diagram for Lead Zirconate-Lead Titanate With 1% Nb_2O_5	15
7	Pressure Versus Temperature Phase Diagram for $Pb_{.995}Nb_{.01}(Zr_{.95}Ti_{.05})_{.99}O_3$ as Developed by Berlincourt and Krueger	18
8	Edge-To-Edge Test Sample Configuration Used by Hall in the Tetrahedral Anvil Device	22
9	Face-to-Face Test Sample Configuration Used by Lees in the Tetrahedral Anvil Device	22
10	Face-to-Vertex Test Sample Configuration Used by Decker in Tetrahedral Anvil Device	22
11	The 600/2400 Ton Tetrahedral Anvil Apparatus Along With the Control Panel and the Low Voltage Looping Module Used for These Studies	23
12	Cross-section of Test Capsule as Positioned in Pyrophyllite Tetrahedron	25
13	Schematic of Hysteresis Looper Used for Poling and Looping Ferroelectric Specimens	26

ILLUSTRATIONS

Figure		Page
14	Charge Versus Potential Poling Trace for PZT 95/5 Ferroelectric Ceramic	29
15	1 kHz Small Signal Relative Dielectric Constant Versus Pressure for PZT 95/5 Ferroelectric Ceramic	31
16	Polarization Versus Electric Field Hysteresis Loop on a Thermally Depoled PZT 95/5 Ferroelectric Ceramic	32
17	Remanent Polarization and Coercive Voltage Versus Pressure as Measured From Hysteresis Loops on a PZT 95/5 Ferroelectric Ceramic	34
18	Polarization Versus Voltage Hysteresis Loops Illustrating How Looping Can Induce the AFE Phase at or Near the Transition of a PZT 95/5 Ferroelectric Ceramic	34
19	Relative Dielectric Constant Versus Pressure for PZT 95/5 Ferroelectric Ceramic	35
20	A Typical Polarization Versus Pressure Poling Trace Near the FE-AFE Transition	35
21	1 kHz Small Signal Relative Dielectric Versus Pressure for PZT 95/5 Ferroelectric Ceramic	37
22	1 kHz Relative Dielectric Constant Versus Pressure for PZT 95/5 Ferroelectric Ceramic	38
23	1 kHz Relative Dielectric Constant Versus Pressure of PZT 95/5 Ferroelectric Ceramic	39
24	Pressure Versus 1 kHz Dielectric Constant in the AFE Phase for PZT 95/5 Ceramic	41
25	1 kHz Relative Dielectric Constant Versus $1/(p-p_o)$ Demonstrating That a Curie-Weiss-Like Relationship Is Followed for This Ceramic in the AFE Phase	42
26	Pressure Versus the Reciprocal of the 1 kHz Relative Dielectric Constant for High Pressure Examinations of Three PZT 95/5 Ceramic Samples	44
27	1 kHz Relative Dielectric Constant Versus $1/(p-p_o)$ for PZT 95/5 Ceramic	45

ILLUSTRATIONS

Figure		Page
28	Components of Complex Dielectric Constant (K' and K'') Plotted on Complex Plane at Various Pressures	46
A-1	Schematic of Tetrahedral Anvil Apparatus Pressurization System	50
B-1	Location of Steel Holding Rod on Pyrophyllite Prism	56
B-2	Configuration of Backup Plate Used to Hold Tetrahedron for Fabrication of Test Specimen Cavity	56
B-3	Position of Tetrahedron Support Assembly on Bed of Wafering Machine	57
C-1	Configuration of Polyethylene Bobbin Used to Support Manganin Wire	59
C-2	Positioning of Bobbin in Pin Vise in Preparation for Winding Manganin Wire	60
C-3	Location of 0.18-mm-Dia. Holes in Bobbin	60
C-4	Method of Holding Manganin Wire to Bobbin by Feeding Through Two 0.18mm-Dia. Holes	61
E-1	Dimensions of 304 Stainless Steel Capsule Used To Contain Sample, Manganin Gage and Fluid	63
E-2	Configuration of Polyethylene End Plug	64
E-3	Location of Lead Wire Holes in End Plug as Viewed From the End on the Outside of the Capsule and the End on the Inside of the Capsule	65
E-4	A Possible Preferred Lead Wire Location in End Plug Which Has the Advantage That the Sample Lead Wires Are Positioned Symmetrically on the Plug	66
E-5	The Final Configuration of the Polyethylene Bottom End Plug With Lead Wires in Place	66
G-1	Attachment of Manganin Wire to Current-Potential Lead Wire	69
G-2	Technique Used to Install End Plug in Capsule	70

ILLUSTRATIONS

Figure		Page
H-1	Cross-section of Test Cell Configuration Used to Calibrate Manganin Gage Using Bismuth	73
H-2	Variation of Manganin Gage Electrical Resistance During Pressurization Cycle	74
H-3	Variation of Manganin Gage Electrical Resistance During Depressurization Cycle	74

TABLES

Table		Page
1	Real and Imaginary Complex Dielectric Constant Components of PZT 95/5 Ferroelectric Ceramic When Tested at Four Test Frequencies at Pressures Up to 3.67 GPa	47

INTRODUCTION

The objective of this study was to experimentally determine the static high pressure dielectric characteristics of a niobium doped 95 percent lead zirconate - 5 percent lead titanate ferroelectric ceramic*. These data can be applied to mathematical models depicting the depolarization of ferroelectric ceramics in an intense high pressure (shock) environment. Since the investigation involved the application of strong electric fields to minute samples at high pressures, new experimental techniques had to be developed.

Although ferroelectric materials are most commonly used as acoustic transducers, the present study concerns a unique application, reported by Nielson[1] in 1956, termed shock depolarization. Nielson indicated that large quantities of charge could be released by stressing the ferroelectric with a shock wave having an intensity above a certain threshold pressure.

An important ferroelectric material used in shock depolarization applications is a niobium-doped ceramic composed of 95 percent lead zirconate and 5 percent lead titanate, commonly known as PZT 95/5. On the lead zirconate-lead titanate composition-temperature phase diagram, a ferroelectric (FE) phase near the PZT 95/5 composition is adjacent to an antiferroelectric (AFE) phase. For PZT 95/5, depolarization is brought about by the pressure inducement of the first-order FE-AFE polymorphic phase change. Under isostatic pressure, this transition occurs at 0.25 to 0.5 GPa, which is considerably below the pressure usually applied during shock depolarization. For undoped PZT 95/5, the composition-temperature phase diagram, although basically straightforward, becomes complex near the Curie temperature (227°C) where another AFE phase is in close proximity[2,3]. During shock depolarization, where there is an adiabatic temperature increase at the shock front, it is possible that both AFE phases along with the paraelectric phase would be encountered.

The characterization of materials such as PZT 95/5, which contain four to five major elements along with dopants and impurities, is difficult because of inhomogeneities and density variations. Further, the electrical response is influenced by variations in grain size, void size, and/or material phase changes. As an electrical circuit component, the shocked ferroelectric exhibits an electrical impedance that varies with pressure and time. Modeling of this process has been examined by Anderson[4],

---

*All compositional percentages in this study are in atomic percent unless otherwise stated.

Lysne and Percival[5], Chen and McCarthy[6], and others. Recent work[7] has been carried out on a shock depolarization model that will depict the electrical response of PZT 95/5 when shocked up to 3.5 GPa. An adequate description of the high pressure properties of this material was available with the exception of permittivity. Due to the difficulty in determining this property dynamically, it has been proposed that static measurements be made and adapted to the dynamic mode. This constitutes the basis for the present study.

In this program, only the ambient temperature static pressure field was investigated. It is believed that these data will suffice for a first-order approximation of the dielectric-pressure response and the corresponding temperature behavior will be left for future researchers.

A tetrahedral anvil apparatus belonging to the Materials Science Department, University of Florida, Gainesville was used to obtain the high static pressures required for these studies. This unit had not been in operation at the University of Florida prior to these tests; thus, this study constituted the first to be performed using the press. Operating instructions are included in Appendix A for future experimenters.

Prior to the initiation of the study it was felt that the ultimate pressures desired were 2.5 to 3.0 GPa. On two occasions the upper end of the Heise gage was approached to examine the capability of the unit (the second time resulted in a broken anvil). However, the ultimate pressure recorded by the internal Manganin cell barely exceeded 4.5 GPa, whereas it was hoped that 6 to 7 GPa could have been attained. Attempts at improving pressure transmission were not performed since the lower pressures were suitable for this study.

A relative dielectric constant based on small signal measurements as well as on high voltage poling measurements was determined as a function of pressure. These data have direct application to simpler shock depolarization models where average values in the shocked and unshocked regions are sufficient. More refined models require dielectric relaxation parameters which consist chiefly of a continuum of frequency-dependent data from the instantaneous to the static dielectric constant. The measuring frequencies were limited to less than 1 MHz. This appeared to be sufficient to determine the static dielectric constant, but instantaneous values were not determined because of the large interpolation error. Thus, it is recommended that further dielectric examinations be made at higher frequencies.

Other items of interest were found which may not have a direct application to depolarization models but broaden the understanding of the depolarization process and dielectric characteristics of PZT 95/5. Prior to the 0.32 GPa FE-AFE transition, the material state (although predominantly FE) appeared to be mixed FE and AFE. High voltage looping provided the activation energy necessary to partially stabilize and induce a portion of the AFE phase. It was possible to induce the entire AFE phase by continued looping at a pressure approximately 0.11 GPa lower than when not looped. Thus, it is paradoxical that an electric field causes the material to favor the FE state but induces the AFE state.

From an analysis of data on a single sample, it was found that the dielectric constant immediately after the transition follows a Curie-Weiss-like relationship similar to that found in other ferroelectrics in the nonpolar paraelectric state.

A discontinuity in the dielectric behavior was detected on all samples at about 2.2 GPa. Initially this was believed to be a phase change, but since then, it has been attributed to pore collapse in the ceramic.

BACKGROUND

PROPERTIES OF DIELECTRICS

When a dielectric is inserted between two parallel plate electrodes, whose capacitance in air is C_o, the capacitance C is increased by $\varepsilon_s/\varepsilon_o$ or K where ε_s is the permittivity or static dielectric constant, ε_o is the permittivity of free space ($8.85 \times 10^{-12} n^{-1} \cdot coul^2 \cdot m^{-2}$) and K is the relative dielectric constant. If the charge Q is maintained constant, then the voltage V across the capacitor is reduced (i.e., $V = Q/C = Q/KC_o$) with the dielectric inserted. The fraction of the charge contributing to the voltage increase (Q/K) is called the free charge while the remainder (Q - Q/K) is called the bound charge.

If charge displacement has occurred in a dielectric, it is said to be polarized and the atoms or molecules within the dielectric are said to possess an induced dipole moment whose magnitude depends on the charge and displacement. The dipole moment per unit volume at a point is called the electric polarization $\vec{P}$. In reference to induced charges on surfaces perpendicular to the polar direction, polarization can also be thought of as charge per unit area.

Polarization is a field vector representing the bound charge density in the dielectric while another field vector, called the electric flux density $\vec{D}$ or dielectric displacement, represents the total charge across the dielectric (i.e., both the bound charge and the free charge). For two parallel plates in a vacuum $\vec{D} = \vec{E}$ (where $\vec{E}$ is the electric field intensity) but with a dielectric inserted, the following results:

$$\vec{D} = \varepsilon_s \vec{E}. \tag{1}$$

The dependence of polarization on electric field and flux density is as follows:

$$\vec{P} = \vec{D} - \varepsilon_o \vec{E} = (\varepsilon_s - \varepsilon_o) \vec{E} = \chi \varepsilon_o \vec{E} \tag{2}$$

where χ, the dielectric susceptibility, is the ratio of the bound charge density to the free charge density. Susceptibility is formally defined as $\partial\vec{P}/\partial\vec{E}\varepsilon_o$, while the relative dielectric constant is $\partial\vec{D}/\partial\vec{E}\varepsilon_o$. In terms of susceptibility the relative dielectric constant is

$$K = \chi + 1. \tag{3}$$

For a dielectric in an alternating field both $\vec{P}$ and $\vec{D}$ vary periodically with time but generally lag behind $\vec{E}$ so that in complex notation if

$$\vec{E}^* = \vec{E}_o \exp (i \omega t) \tag{4}$$

then

$$\vec{D}^* = \vec{D}_o \exp [i(\omega t - \delta)] \tag{5}$$

where ω is the angular frequency and δ is the phase difference. From Equation No. 1, it follows that a complex permittivity relates $\vec{D}^*$ and $\vec{E}^*$, i.e.,

$$\vec{D}^* = \varepsilon^* \vec{E}^* \tag{6}$$

and

$$\varepsilon^* = \vec{D}_o \vec{E}_o^{-1} \exp (-i\delta) = \varepsilon_s(\cos \delta - i \sin \delta). \tag{7}$$

It is seen that the ratio $\vec{D}_o \vec{E}_o^{-1}$ is frequency dependent with two frequency dependent permittivities $\vec{D}_o \vec{E}_o^{-1}$ sin δ and $\vec{D}_o \vec{E}_o^{-1}$ cos δ (permittivity is also temperature dependent). These are generally expressed using the single complex permittivity as follows:

$$\varepsilon^* = \vec{D}_o \vec{E}_o^{-1} \cos \delta - i \vec{D}_o \vec{E}_o^{-1} \sin \delta = \varepsilon' - i \varepsilon''. \qquad (8)$$

In this equation ε' is called the permittivity, while ε'' is the loss factor. It can be shown that the heat dissipated in a dielectric is proportional to ε''. It is seen that the ratio $(\varepsilon''/\varepsilon')$ equals tan δ; this is called the dissipation factor and if the permittivity (ε') and dissipation factor are known, then the loss factor ε'' can be determined (i.e., $\varepsilon'' = \varepsilon' \tan \delta$).

In a time varying, dynamic electric field, the response of dielectrics can be treated in a manner similar to the response of other materials under dynamic conditions, i.e., if a field is suddenly applied to a dielectric, the static permittivity will not be attained immediately due to the inertia of polarization, but will increase gradually to ε_s after it has attained an instantaneous value denoted by ε_i. The latter follows the electric field immediately and is called the instantaneous or optical permittivity (this is the permittivity at infinite frequency).

A well-established relaxation model proposed by Debye which makes use of the Principle of Superposition and the fact that polarization can be described by an exponential law of the form exp $(-t/\tau)$ with a single relaxation time (τ) has gained wide acceptance because Debye was able to show how the results could be applied to a simple molecular model. By a straightforward derivation,[8] relationships known as the Debye equations were obtained which expressed complex permittivity in terms of ε_s, ε_i, ω and τ. These equations are as follows:

$$\varepsilon^* = \varepsilon_i + (\varepsilon_s - \varepsilon_i)(1 + i\omega\tau)^{-1} \qquad (9)$$

$$\varepsilon' = \varepsilon_i + (\varepsilon_s - \varepsilon_i)(1 + \omega^2\tau^2)^{-1} \qquad (10)$$

$$\varepsilon'' = (\varepsilon_s - \varepsilon_i)(\omega\tau)(1 + \omega^2\tau^2)^{-1} \qquad (11)$$

Experimentally, as a periodic field is applied to a dielectric, the capacitance and dissipation factor are the usual parameters which are measured as a function of frequency. A method of representing and analyzing these data which is attributed to Cole and Cole,[9] is based on plotting the real and imaginary part of the complex permittivity in the complex plane (ε' versus ε''). Each point then represents one frequency measurement and the locus is a semicircle (for a single relaxation time) as ω varies from 0 to ∞ with its ends intersecting the real axis at ε_i and ε_s. For experimental data which cover the in-between regions of absorption and dispersion, the Cole-Cole plot constitutes a method for determining ε_i and ε_s by extrapolation. For a model representing a distribution of relaxation times the locus is still circular in shape with a chord of the circle lying on the real axis having ε_i and ε_s at the extremities of the chord.[9]

The subject of dielectric dispersion and adsorption in ferroelectric materials is of considerable interest particularly in connection with ferroelectric transitions. Several references are available which treat this subject in more depth than will be presented here. As applied to shock depolarization, it is understood that dielectric relaxation characteristics are of considerable importance in treating advanced models[7].

The relationship between polarization and electric field is one of the most distinguishing characteristics of ferroelectrics. By using a simple circuit devised by Sawyer and Tower,[10] $\vec{P}$ and $\vec{E}$ can be displayed directly on the coordinates of an XY recorder or oscilloscope. It is observed that the polarization-field relationship is not only nonlinear but, if a sufficiently strong field is applied in the positive and then negative direction, hysteresis results.

For the remainder of this study, the vectorial symbol, $\rightarrow$, will be omitted since in this study the electric field and polarization vectors will always be normal to the electrode surfaces.

FERROELECTRICITY

Ferroelectric materials exhibit spontaneous polarization, meaning that they possess an electric dipole moment in the absence of an electric field. However, the distinguishing property that classifies a material as being ferroelectric is that the direction of spontaneous polarization, called the polar axis, can be reversed by a sufficiently strong electric field.

One of the most prominent characteristics of ferroelectric materials is the charge-field hysteresis loop. Figure 1, which is a typical "loop," illustrates hysteresis along with the well-known nonlinear relationship between polarization and electric field.

For materials which exhibit hysteresis, equations of state relationships are difficult to establish because processes which exhibit hysteresis behavior are irreversible; thus, parameters cannot be equated by a unique functional relationship. For ferroelectric materials (Figure 1), the intensive parameter (E) is plotted along the abscissa while the extensive parameter (P) is along the ordinate. The trace on most virgin ferroelectrics or on most that have been thermally depoled follows the curve OAB but thereafter as the field varies from E_m to $-E_m$ the curve BCDFGHB is followed. When E is finally reduced to zero, remanent polarization of magnitude P_r (or $-P_r$) remains as bound charge in the ferroelectric. Curve OIB, called the medium line, is a tracing similar to that plotted by the initial trace on a ferroelectric after it has been pressure depoled.

Certain features which help to characterize ferroelectric materials can be defined from the hysteresis loop. Extrapolation of the linear portion of the tracing above saturation to the ordinate defines the macroscopic spontaneous polarization P_s. The value of polarization where the loop intersects the ordinate is called the remanent polarization, P_r. The electric field at which the ferroelectric becomes saturated is denoted by E_s, while the electric field required to reduce the polarization to zero is the coercive field, E_c.

For most ferroelectrics, the polar state exists only below a certain temperature or in a temperature range. Above this temperature, which is known as the Curie temperature, T_c, the ferroelectric loses its bound charge and transforms to the nonpolar paraelectric (PE) phase. Due to the nonlinear field-polarization behavior, the dielectric constant is usually defined as the slope at the origin (exceptions to this definition are made in this study; however, such exceptions are noted). The dielectric constant increases up to the Curie temperature, at which time it decreases. The Curie temperature is thus defined as the temperature at which the dielectric constant peaks.[11] For many ferroelectrics the Curie temperature varies depending on whether or not it is being heated or cooled.

Above T_c, in the nonpolar paraelectric state, the dielectric constant is described by the Curie-Weiss law,

$$\varepsilon = C/(T - T_o) \qquad (12)$$

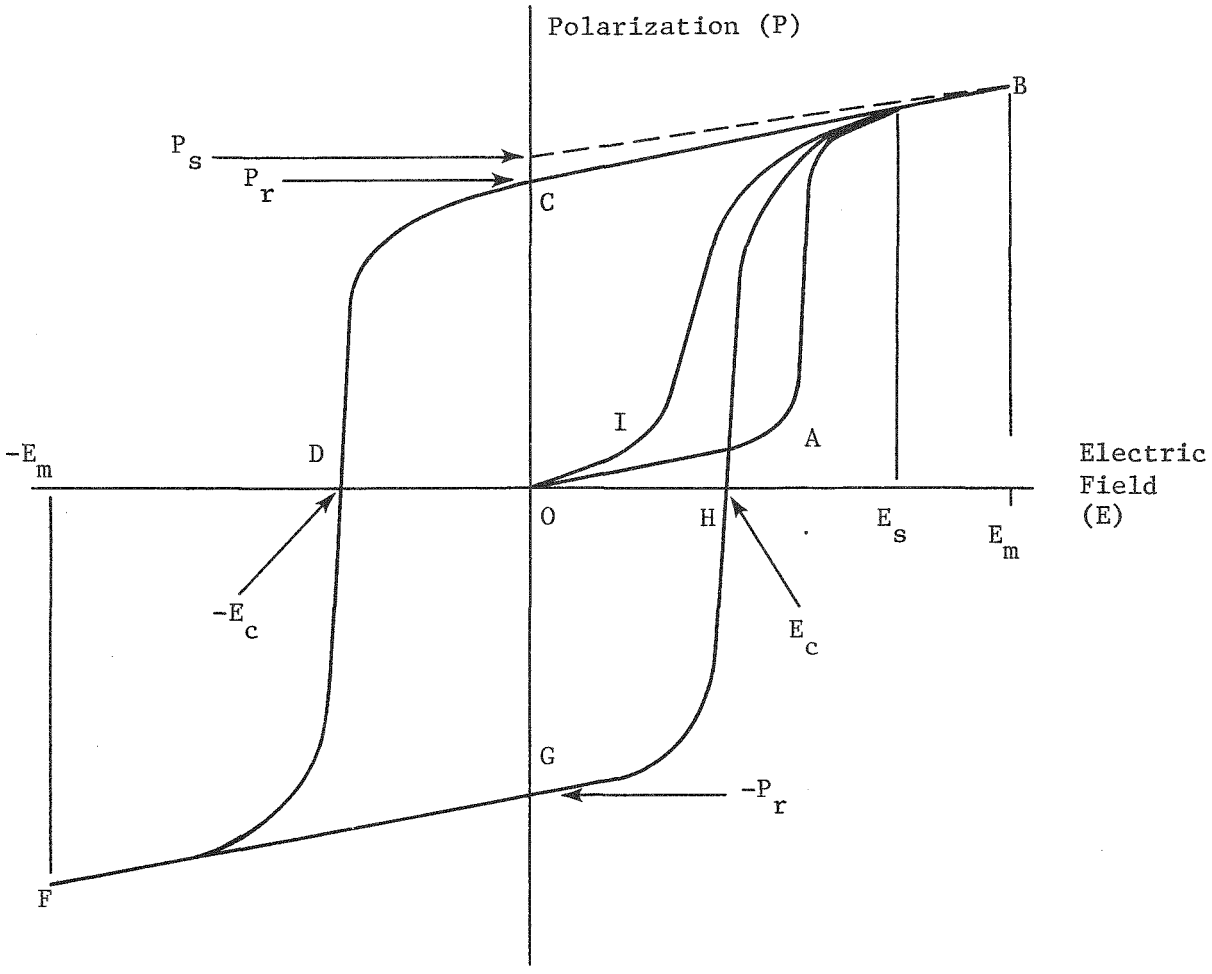

Figure 1. Typical Polarization Versus Electric Field Hysteresis Loop for Ferroelectric Materials

where C is the Curie constant and T_o is the Curie-Weiss temperature. The Curie temperature is defined as the temperature at which $1/\varepsilon$ extrapolates to zero when plotted against temperature. In most ferroelectrics T_o coincides with T_c; however, there are compositions in which it may be a few degrees below.[11]

Most ferroelectric ceramics used in technical applications belong to a structural class called the oxygen octahedral group. The unit cell configuration of these ceramics for the most part is the perovskite subgroup having the chemical formula ABX_3. Although the perovskite unit cell is cubic in the nonpolar phase, atomic displacements which cause a slight distortion as it is cooled through T_c result in less symmetric structures which are either tetragonal, orthorhombic or rhombohedral.

On a microscopic scale the ferroelectric structure consists of small ordered regions for which the polarization vector of each dipole is oriented in approximately the same direction. These regions are called domains and a monocrystal or crystallite (if the material is a ceramic) may consist of many domains as subcells within each grain which appear under magnification as crystallographic twins. For two or more adjacent domains the magnitude of spontaneous polarization is essentially identical; however, the polar axis differs.

In a virgin ferroelectric, the macroscopic spontaneous polarization is zero due to the randomness of the domain polarization direction. As an electric field is applied, the ferroelectric initially behaves as a normal dielectric (from 0 to A in Figure 1); however, as the field increases, domains with a polarization vector closely aligned with the field grow at the expense of nonoriented domains (from A to B in Figure 1). Eventually the polarization vector of each domain in the material is aligned as closely as possible with the polar axis and $\partial E/\partial P$ is constant. Energetic considerations involving domain formation are quite complex due to the fact that domain occurrence is preceded by a nucleation and growth mechanism. Activation energies required for movement and switching can be of considerable importance.

Ferroelectric ceramics became functional as a result of the orientation of domains to favor a selected direction. This is performed by a process known as poling which consists of aligning domains by increasing the electric field to a point above E_s. The ferroelectric is then left in a poled state with a net bound charge equal to P_r.

Domain alignment is associated with the degree of freedom possessed by the B site atom (the center atom) in the perovskite unit cell. In the polar phase, 180° domain reorientation is possible for all structures. Along with 180° switching, domains may reorient by 90° for tetragonal and orthorhombic, 60° to 120° for orthorhombic, or 71° or 109° for rhombohedral.[12] The orientation of all domains except 180° domains results in an overall distortion of the ferroelectric; consequently, the coercive voltage is less for this type of reorientation. All domains are reoriented during the first few hysteresis loop cycles but thereafter only 180° reorientation. The difference between curve OAB and OIB of Figure 1 is due to the fact that 180° domain switching predominately occurs for curve OIB while 90° and 180° switching occurs for OAB.

Energy conversion in ferroelectrics is attributed to three processes: (1) piezoelectric conversion, consisting of the linear and reversible coupling between elastic and dielectric energy, (2) stress or temperature depolarizing effects due to reorientation of domains, and (3) forced phase transition depolarization in which bound charge is released by applying sufficient pressure to cause the FE phase to transform to a PE or AFE phase. The latter two processes are nonlinear and irreversible. Energetic considerations for all three mechanisms are discussed by Berlincourt.[13] The present study is concerned in part with the third mechanism, i.e., energy conversion by phase transitions.

The AFE transition is one which was theoretically predicted and explained by Kittel[14] prior to its realization. These materials transform from a nonpolar state to one known as antipolar. Where it is possible in a FE phase to have other than 180° domain reorientation, in an AFE phase only 180° are present. While these subcells are polar, the adjacent subcells are oppositely polarized giving a net polarization of zero. Domain alignment is such that these materials possess a center of symmetry; as a consequence, they are not piezoelectric.

At the AFE-PE transition, the free energy of the AFE phase for many of these materials is close to that of an FE phase. Under these circumstances it may be possible to enforce the FE phase with an electric field. For this situation a plot of P versus E results in what is known as a double hysteresis loop (Figure 2). Not all AFE materials exhibit this behavior; one that does is termed "soft."[15] The field at which the FE phase is switched (designated as E_A) increases as the free energy between the AFE and FE states widens until the dielectric breakdown strength is exceeded.

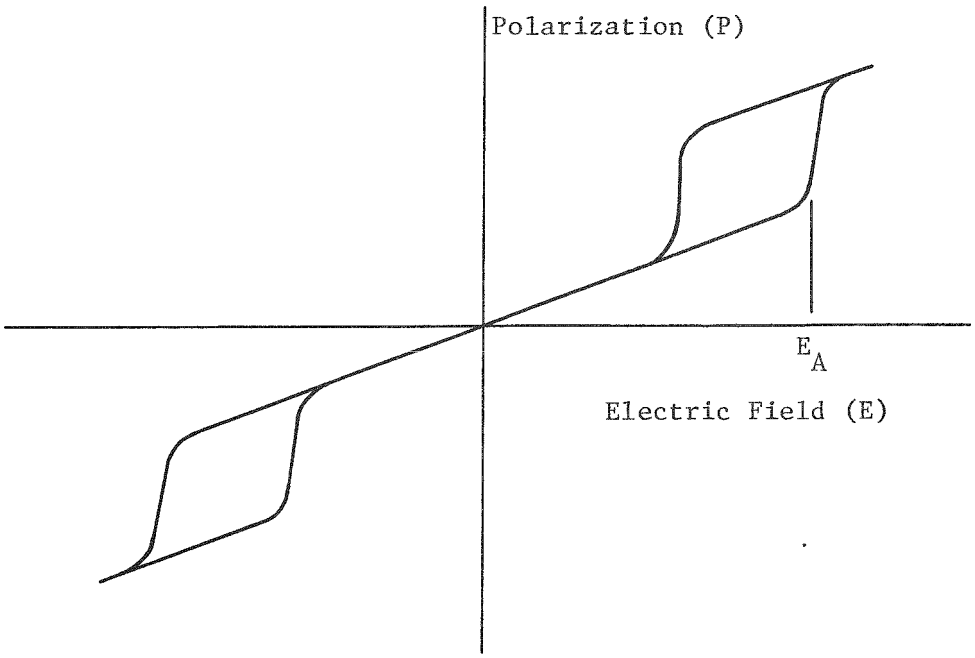

Figure 2. Polarization Versus Electric Field for an Antiferroelectric Material With Field Enforced Ferroelectricity

Like FE materials, many AFE materials show a high dielectric constant peak near the polar to antipolar transition temperature. It has been suggested that this peak is not associated with the AFE state, but is attributed to the closeness in free energy between the FE and AFE phases at T_C.[16]

Double hysteresis loops not attributed to antiferroelectricity are observable in FE materials that exhibit a polarization change as a result of a bias above T_C. A typical field-temperature phase diagram for such materials is shown in Figure 3. An FE at temperature T_1 would exhibit a normal hysteresis loop, while the same material at T_2 would exhibit the double loop. Thus, the recognition of an antiferroelectric material can be difficult since there appear to be no dielectric test methods that specifically confirm the AFE state. In situations where doubt exists, proof is established by a detailed structural analysis and this information along with dielectric measurements can be used to classify it.[17]

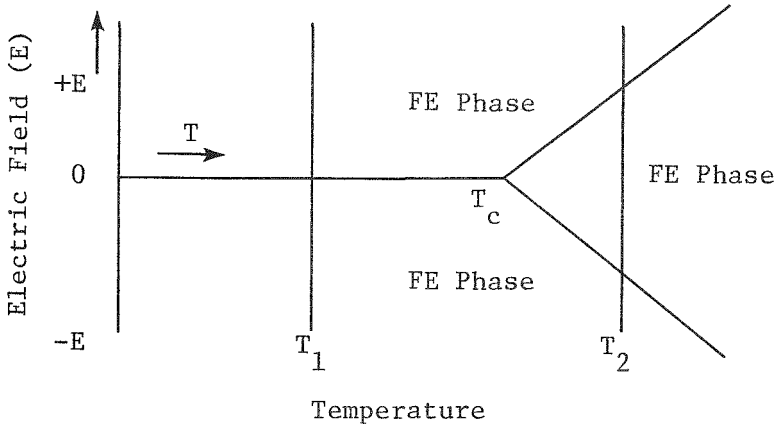

Figure 3. Electric Field Versus Temperature Showing Phases Encountered for Some Ferroelectric Materials When Looped at T_1 and T_2. At T_2 a double hysteresis loop may result even though the material is not AFE.

FERROELECTRIC COMPOSITION PZT 95/5

In 1953, Sawaguchi[18] presented a PZT temperature-composition phase diagram similar to that shown in Figure 4. The most studied compositions lie near the 50-50 morphotropic phase boundary because of the enhancement of the piezoelectric properties as this boundary is approached. In Figure 4, the dotted line designating the FEI-FEII boundary in the FEA phase was first noted by Barnett.[19] At this boundary there is a dielectric anomaly and a change in thermal expansion; however, X-ray analysis shows the structure on either side to be rhombohedral.[19]

PZT 95/5 was developed primarily for shock depolarization purposes. As seen in Figure 4, the composition is in close proximity to the AFE-FE polymorphic phase boundary. With pressure the phase boundary is caused to displace to the right; i.e., the AFE phase is preferred over the FE phase.

The peculiar polarization behavior of lead zirconate was first observed by Roberts[20] in 1950. However, it has been noted[21] that Sawaguchi was the first to describe its behavior as antiferroelectric. In Sawaguchi's 1953 paper[2], the properties of lead zirconate with small quantities of lead titanate as determined by structural analysis, dielectric measurements, heat capacity measurements, and dilatometry were presented. In the tetragonal antiferroelectric phase (AFE_B), it was shown that it was possible to enforce ferroelectricity which resulted in a double hysteresis loop. This was not possible for the AFE_A phase. Additional phase diagram studies made by Berlincourt and Krueger[22] showed that the AFE_B phase was observed only on tests made with increasing temperature.

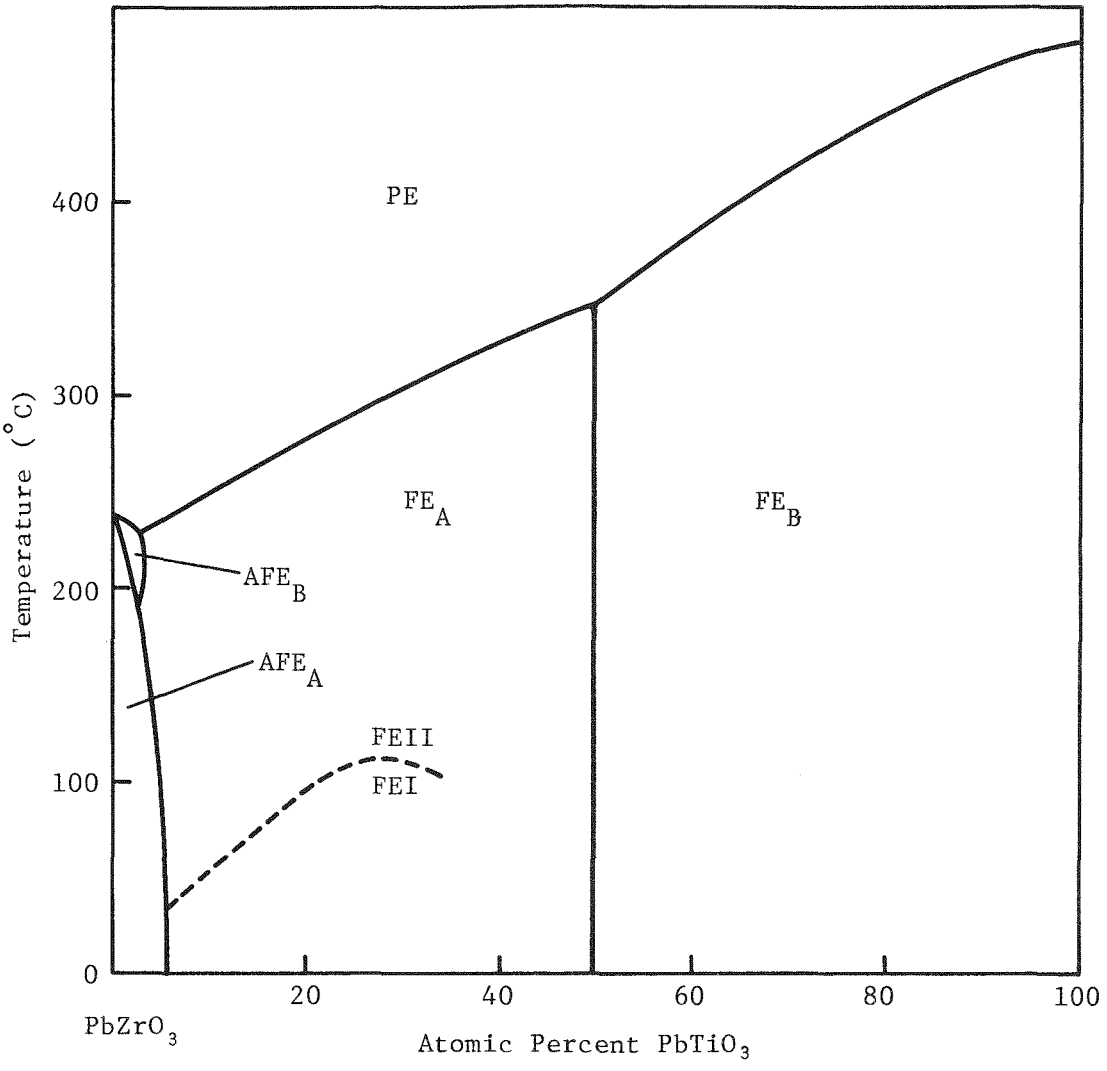

Figure 4. Temperature Versus Composition Phase Diagram for Lead Zirconate-Lead Titanate (No Niobium). This plot is similar to that developed by Sawaguchi[23] except for the added FEI-FEII boundary noted by Barnett.[19]

These phase diagrams as well as similar diagrams on other ferroelectric materials show two phases separated by a single line rather than a two-phase region as required by the Gibbs phase rule. Jaffe et al[24] have confirmed that two phases actually are in equilibrium between the FE_A and FE_B phases of PZT, but because of the narrowness of the boundary, detection methods usually result in a single peak. This is partially due to a metastable phase which transforms rapidly after it is initiated. To be more descriptive, some authors refer to these diagrams as "transitive temperature-composition" diagrams.

For the present project the specific PZT composition is $Pb_{.995}(NB_{.01}(Zr_{.95}Ti_{.05})_{.99})O_3$. This is commonly referred to as PZT 95/5 with 1 percent niobium, or just PZT 95/5. Niobium in small percentages is added to many PZT ferroelectric ceramics to improve electrical resistance at high temperature. For PZT 95/5 it was found that by varying Nb_2O_5 between 0.5 and 1.5 percent, the depoling pressure varied directly. However, because of fluctuations in manufacturing methods, chemical impurities, pore size, grain size, etc., the precise dependence of depoling pressure on Nb_2O_5 was difficult to establish. In order to obtain a composition with a desired depoling pressure, it was necessary to adjust the niobium content on a small portion of a large batch until the correct depoling pressure was attained; the remainder of the batch was then corrected and processed. For this reason the exact amount of niobium present in the ceramics used in this study was not known.

The effects of niobium on the PZT system near the pure lead zirconate composition has been examined by Dungan et al,[25] Berlincourt and Krueger,[22] and Torccaz et al.[26] The room temperature ternary diagram of compositions between 100% $PbZrO_3$, 10% $PbTiO_3$, and 10% $PbNb_2O_6$ determined by Dungan et al[27] is shown in Figure 5. As niobium increases, the FE phase of a composition containing 5% $PbTiO_3$ becomes further from the AFE phase which is what would be expected from pressure depolarization results reported by Berlincourt and Krueger.[22]

A lead zirconate-lead titanate compositional-temperature phase diagram with 2.5% Nb by Dungan et al[28] and diagrams by Berlincourt and Krueger which contain 1% Nb[29] and 2% Nb[30] do not show the AFE phase. This indicates that this phase is possibly nonexistent for PZT materials containing niobium. However, a low temperature AFE phase appears in the compositional-temperature phase diagram developed by Torccaz et al.[26] The significance of this is not known; it is believed that the phase occurs only upon cooling.

The 1% Nb phase diagram developed by Berlincourt and Krueger[31] along with the Torccaz et al 1% Nb diagram[32] is shown in Figure 6.

Figure 5. Ternary Compositional Phase Diagram at Room Temperature for $PbZrO_3$, $PbTiO_2$, and $PbNb_2O_6$ Near the 100% $PbZrO_3$ Composition[27]

Figure 6. Temperature Compositional Phase Diagram for Lead Zirconate-Lead Titanate With 1% Nb_2O_5. As developed by Berlincourt and Krueger[29] as shown by solid lines, and by Torccaz et al[32] as shown by dashed lines.

FERROELECTRICS AT HIGH PRESSURE

Pressure effects on the properties of ferroelectrics have been examined using both static (hydrostatic and quasihydrostatic) and dynamic (stress waves and shock waves) techniques. Because of the pressure-sensitive characteristics of ferroelectrics, the use of static techniques has been a popular area of investigation. Earlier static experimental studies have been confined to relatively low pressures (< 1 GPa). However, within the last 15 years higher pressure results have been reported.

Pressure investigations on ferroelectrics have been most extensively performed on barium titanate. Samara[33] has investigated the effect of both pressure and temperature on monocrystals as well as polycrystalline $BaTiO_3$ up to 2.5 GPa. He found that for both types of samples, the Curie temperature decreased linearly with pressure.[33] However, an interesting difference between the samples was observed; the permittivity of the monocrystal (taken along with the "c" axis) increased near the FE-PE transition by 60 to 70 percent as pressure increased up to 1.5 GPa while that of the ceramic decreased by over 50 percent in the same pressure range. It appears that this is related to the pressure dependence of the permittivity along the "a" axis (ε_a). For these measurements ε_c, not ε_a, was determined on the monocrystal and since the length of the "c" axis decreases with pressure faster than the "a" axis, it is reasoned that domains in the "c" direction switch to the "a" direction, causing ε_c to increase. For the macroscopically isotropic ceramic, an average value of ε is measured. Ceramic porosity was not considered as a contributing factor because the denser ceramics showed a larger decrease in ε.[11]

Samara found that the permittivity of $BaTiO_3$,[34] $SrTiO_3$,[35] and $PbTiO_3$[36] obeyed a Curie-Weiss type relationship in the high pressure nonpolar (PE) phase, i.e.,

$$\varepsilon = C^*/(p - p_o) \qquad (13)$$

where C^* and p_o are constants with p_o equal to the pressure at which $1/\varepsilon$ extrapolates to zero when plotted against pressure.

It was also observed that for $BaTiO_3$[37] the remanent polarization as well as the coercive field gradually decreased up to the Curie temperature at which time the loop took on the form of a double hysteresis loop.

Examinations above 2.5 GPa have been performed on $SrTiO_3$ (up to 5 GPa) by Samara and Giardini[38] using a tetrahedral anvil device. In these experiments the pressurization medium was AgCl which is considered to be quasihydrostatic at these pressures.

Polandov et al[39] have examined polycrystalline PZT 53/47 with 1% Nb_2O_5 at quasihydrostatic pressures up to 8 GPa. The results showed a gradual decrease in ε from 2 to 2.3 GPa; ε then increased and peaked at a value of 3.6 to 4 GPa and then gradually decreased. The decrease in ε at 2 to 2.3 GPa was attributed to the breakup of the crystallites (due to void collapse) at which time the domain configuration was rapidly changing, causing an anomaly in ε. When the material took on more stable domain configuration, the dielectric constant increased. The reason ε peaked at 3.6 to 4 GPa was not explained.

A limited amount of static high pressure information is available on PZT 95/5. Berlincourt and Krueger,[40] developed a pressure-temperature phase diagram for PZT 95/5 (Figure 7) that showed pressure favoring the AFE phase. At ambient temperature the FE-AFE transition occurred at 0.14 GPa. Hydrostatic studies have been performed by Gonnard et al[41] on a PZT 95/5 type ceramic ($PbZr_{.95}Ti_{.05}O_3 + {.8}WO_3$) in which a transition pressure of 0.18 GPa was reported.

Numerous theoretical studies have been made on the dynamic depolarization mechanisms in ferroelectrics.[1,4,5,6,42] Also, experimental investigations on the effect of shock waves in ferroelectric materials such as $BaTiO_3$, PZT 52/48, PZT 65/36 and PZT 95/5 have been reported.[42,43,44,45,46,47]

Of importance in the experimental studies has been the appearance of a two-wave shock structure; i.e., the wave does not consist of a single step but propagates as two components of different stress amplitudes. This was first noted by Nielson on barium titanate and PZT 52/48 ceramics.[48] Shortly thereafter, Reynolds and Seay[43,44] confirmed these results. Similar observations were seen on PZT 95/5 by Halpin,[42] Doran,[45,46] and Linde.[47] (In one instance a three-wave structure was reported by Doran.)

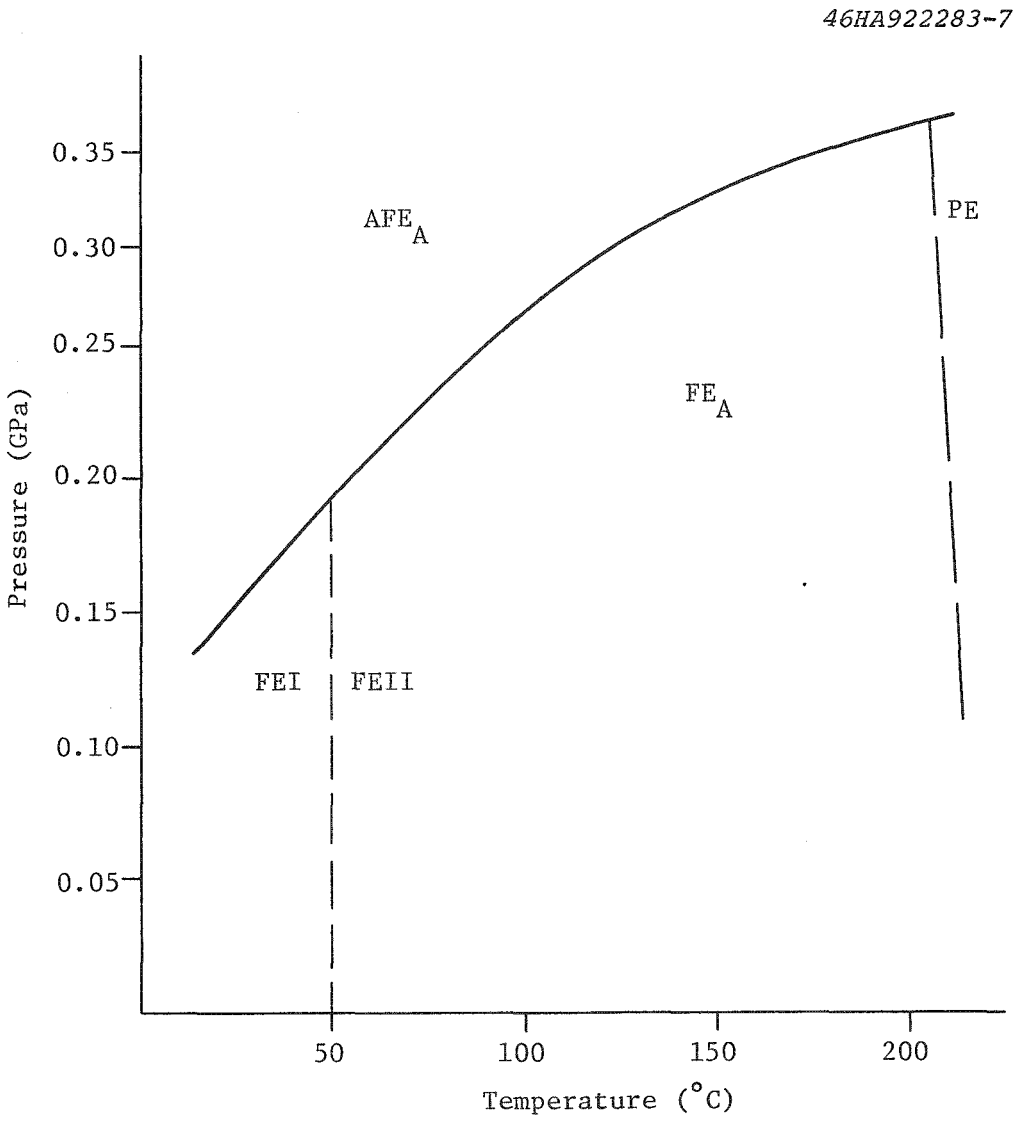

Figure 7. Pressure Versus Temperature Phase Diagram for $Pb_{.995}Nb_{.01}(Zr_{.95}Ti_{.05})_{.99}O_3$ as Developed by Berlincourt and Krueger[40]

Multiple-wave shock structures are attributed to either phase changes or material rigidity. Regarding the former mechanism, numerous examples of shock induced phase transformations were described by Lysne et al[49] in a review of this subject. For $BaTiO_2$ and PZT 52/48, Reynolds and Seay[44] attributed the observed two-wave structure to rigidity effects due to the fact that on samples tested above the Curie temperature, the two-wave structure persisted and when the amplitude of the initial wave was plotted versus temperature, it appeared to be continuous through the Curie temperature. They attribute the loss of remanent polarization to a reduction in dipole moment by axial compression rather than by domain reorientation. As a result of their studies, a Hugoniot was constructed which showed an elastic cusp of 2.3 GPa for $BaTiO_3$ with a steady shock threshold of 48 GPa and for PZT 52/48 an elastic cusp of 1.9 GPa with a steady shock threshold of 21 GPa.

For shock depolarization studies performed on PZT 95/5, Doran[50] found the amplitude of the first wave varied between 2.1 and 4.8 GPa depending on the initial density. Halpin[42] examined PZT 95/5 up to 3.3 GPa and found the first wave amplitude to be 0.5 GPa; thus, he suggested that it was associated with the FE-AFE transition. Except for one sample, all of Halpin's ceramics were hot pressed.

None of the above references mentioned collapse of voids as a possible cause of the multiple-wave shock structure. However, in a recent analytical study, Nunziato and Walsh[51] showed the existence of two distinct acceleration waves in a granular solid with porosity. Using a model for a granular material proposed by Goodman and Cowin,[52] they showed that an acceleration wave moving into such a material would decompose into two waves, one associated with the compressibility of the granules and the other associated with the void collapse. Although that work has not yet been extended to shock and higher-order waves, it is expected that a similar two-wave structure will exist for shock propagation.

HIGH PRESSURE STATIC TEST APPARATUS

Prior to the mid-1950's, ultrahigh pressure testing for the most part had been confined to the flat anvil apparatus developed by P. W. Bridgman. This was a uniaxial piston-anvil device in which the geometry of the tungsten carbide anvils and steel binding rings was such as to provide optimum lateral support to the anvil surface in contact with the specimen. With the complete press under 3 GPa isostatic pressure, it was possible to subject a specimen to over 45 GPa.[53] Much of the success of this unit was attributed to the pipestone (catlinite) compressible gasket used to contain the test specimen.

In 1958, Hall[53] described a three-dimensional press which incorporated the pressure-transmitting features of Bridgman's two-dimensional flat anvil apparatus. This device, called the tetrahedral anvil apparatus, applied uniform pressure to the faces of a regular tetrahedron fabricated from the mineral pyrophyllite*.

Hall selected pyrophyllite over pipestone because it was more readily available and more machinable. However, because pipestone contains iron oxide (known for its high coefficient of friction), it is preferred for ultrahigh pressure testing.

Hall's original design consisted of four hydraulic cylinders or rams positioned so that their anvil faces were parallel with the faces of the tetrahedron while their centerline intersected at the center of the tetrahedron. The rams were held in place with tie-rods. In addition to this tie-rod unit, some variations in the tetrahedral press have been introduced. A popular unit capable of 9.0 GPa, called the NBS unit, was devised by Lloyd, Hutton and Johnson.[54] For this unit, the driving force was applied to a single (upper) anvil rather than all four anvils. The resultant forces were transmitted to the three remaining (bottom) anvils.

Another unit quite similar to the tie-rod unit replaced the ram-tie-rod structure with four steel forgings (called platens) which were connected by hinges. A large diameter cavity in the platen contained a pressure-transmitting piston. This type of unit was called the hinged tetrahedral anvil apparatus and is the type of device used in the present study.

The sample for these pressures was located at the center of the pyrophyllite tetrahedron. Pressure applied to the sample was dependent upon the ability of the pyrophyllite to act as a pressure-transmitting medium without excessively extruding between the anvils. Along with transmitting pressure, the pyrophyllite imparted thermal and electrical insulation and provided material for the necessary gasket. The edges of the tetrahedron were purposely longer than the legs of the triangular face of the anvil so that the gasket could be formed by extrusion of the pyrophyllite between adjacent anvils during the initial pressurization stages. The necessity of the gasket is appreciated when one considers that at high pressures it is possible to subject the tetrahedron to pressure variations from 10 GPa to 100 kPa in a distance of 1 to 2 cm.

---

*Hydrous aluminum silicate ($3Al_2O_3$-$4SiO_2$-H_2O). (Pyrophyllite is also known as wonderstone or Tennessee Grade A Lava, a product of 3M Corporation, Chattanooga, Tennessee).

For pyrophyllite, Hall[55] suggested an edge length 125 percent longer than the anvil triangle legs. This ratio has been confirmed by others.[56] To limit the flow of pyrophyllite at the anvil faces, jeweler's rouge (Fe_2O_3), suspended in an organic solvent, has sometimes been painted on the faces of the tetrahedron. With its high friction coefficient of 0.71,[57] the lateral movement of the pyrophyllite relative to an anvil face was reduced.

The test specimen can be placed within the pyrophyllite tetrahedron in various ways. The three most common configurations are shown in Figures 8, 9 and 10. Figure 8, called the edge-to-edge configuration, resembles Hall's original design.[55] Figure 9, called the face-to-face configuration, has been used by Lees.[58] Figure 10, called the face-to-vertex configuration, was used by Decker et al[59] and can be used to make simultaneous electrical measurements on samples contained within a true hydrostatic pressure environment. This is the sample configuration selected for this study; details of its construction are presented later.

EXPERIMENTAL PROGRAM

TETRAHEDRAL ANVIL APPARATUS

The tetrahedral anvil apparatus along with the control console and an instrumentation module used for this study are shown in Figure 11. This unit* is known as the 600/2400 ton model which designates a device in which a maximum of 600 tons of force can be transmitted by each of the four pistons.

Prior to the initiation of this project, the press had been in storage. The elapsed storage time was unknown but it was suspected that corrosion damage to the pistons or cylinder walls had occurred since the pistons were not removed from the platens prior to storage and since it was known that the manufacturer recommended water (with a rust preventative) as the pressurization medium. Upon removal of all pistons, corrosion damage (as shallow pits) was observed on all cylinder walls with one cylinder showing an extensive amount of damage in the form of two deep corrosion pits. These, as well as the shallow pits, were filled with Epocast 40** tooling epoxy and blended with the cylinder wall using 600 grit emery paper. After reassembling, the hydraulic system was recharged with Harmony 44*** SAE 5 oil.

---

*Fabricated by Barogenics Corp., New York, N. Y.
**Trademark, Furane Plastics
***Trademark, Gulf Oil Co.

46HA922283-8

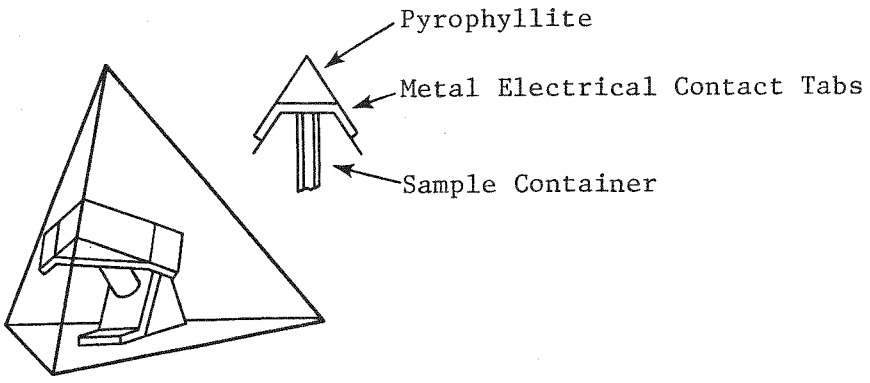

Figure 8. Edge-to-Edge Test Sample Configuration Used by Hall[55] in the Tetrahedral Anvil Device

46HA922283-9

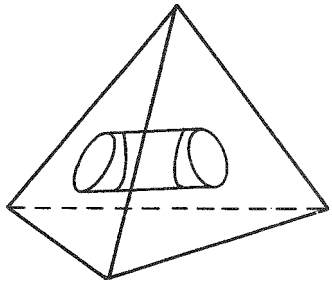

Figure 9. Face-to-Face Test Sample Configuration Used by Lees[58] in the Tetrahedral Anvil Device

46HA922283-10

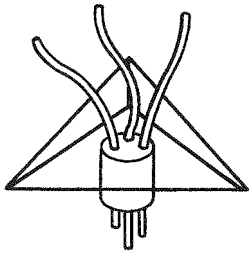

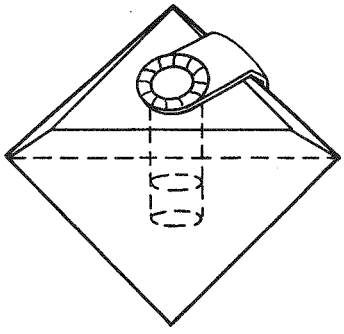

Figure 10. Face-to-Vertex Test Sample Configuration Used by Decker et al[59] in Tetrahedral Anvil Device

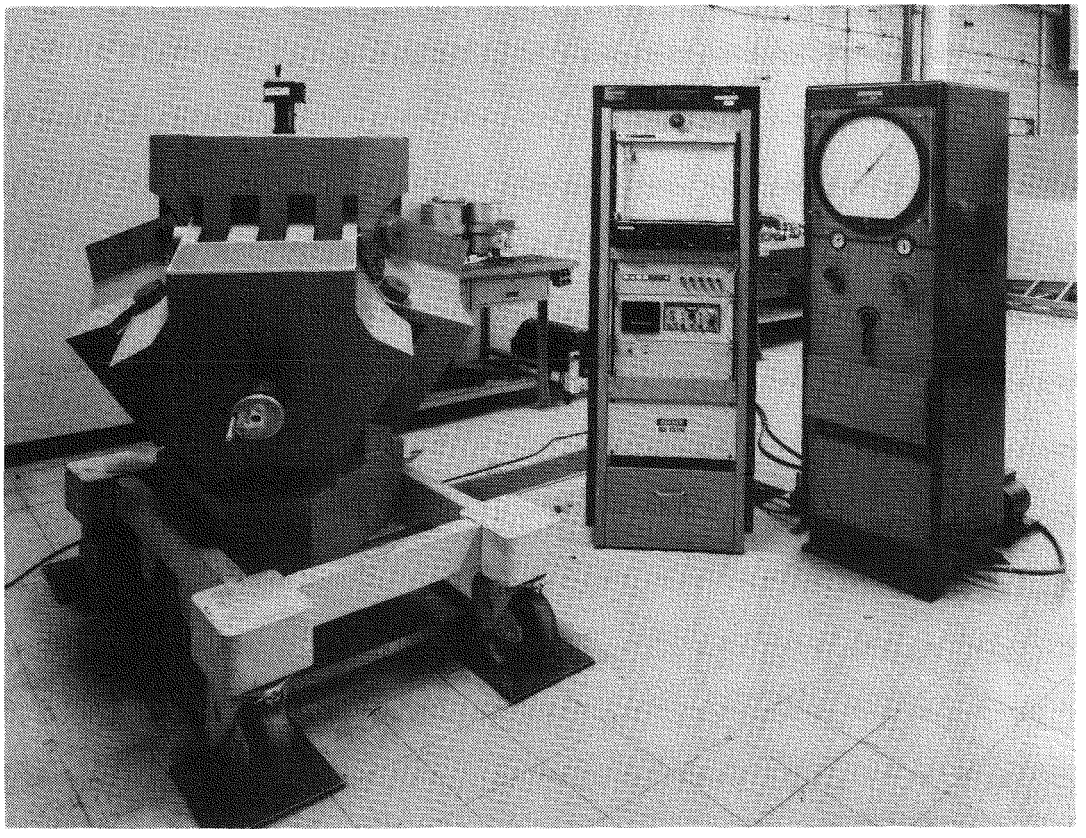

Figure 11. The 600/2400 Ton Tetrahedral Anvil Apparatus Along With the Control Panel and the Low Voltage Looping Module Used for These Studies

A description of the press, along with modification performed on the press and the operation instructions, is given in Appendix A.

TEST CELL

Details concerning the fabrication and assembly of the test cell and tetrahedron, along with information regarding the dielectric fluid, ferroelectric samples and Manganin* are all given in Appendices B through G. The face-to-vertex cell configuration shown in Figure 10 was used for this study. The Manganin cell and FE test sample were positioned in a thin-wall stainless steel cylinder which was filled with a one-to-one mixture by volume of pentane and isopentane and capped at each end with polyethylene plugs. A cross-sectional view of the final test assembly is shown in Figure 12.

INSTRUMENTATION AND MEASUREMENT TECHNIQUE

The resistance of the Manganin cell was determined by applying a 10-mA current to the cell and measuring the voltage drop with a Model HP 3460A digital voltmeter. This has an accuracy of ± 0.002 percent with six place resolution. An HP Model 256** printer was adapted to the voltmeter. This was capable of printing the voltmeter output to five places on demand or at a continuous rate. The current supply (HP351**) used was accurate to ± 0.05 percent; however, prior to and following each test series the actual current was determined by substituting a standard 100-ohm resistor accurate to ± 0.005 percent in place of the Manganin cell.

Charge-field hysteresis loops were performed using a low voltage looper (schematic shown in Figure 13). Peak voltage up to 3000 V could be selected while the looping period could be varied from 28 to approximately 500 seconds. It was possible to subject a sample to an entire loop or merely to pole it. The voltage output with time is linear; thus, a triangular-shaped wave resulted. Two integrating capacitors could be switched in and out of the circuit. A 1.87 μF capacitor was used for looping while a 0.1 μF was used for poling. The trace was recorded on an HP7046A** XY recorder.

---

*Manganin is an alloy whose resistance varies with pressure but not temperature in a range about room temperature. The composition will vary depending on manufacturer. Typical compositions are 87% Cu-13% Mn and 83% Cu-13% Mn-4% Ni where the composition is in weight percent.

**Trademark, Hewlett-Packard Corp.

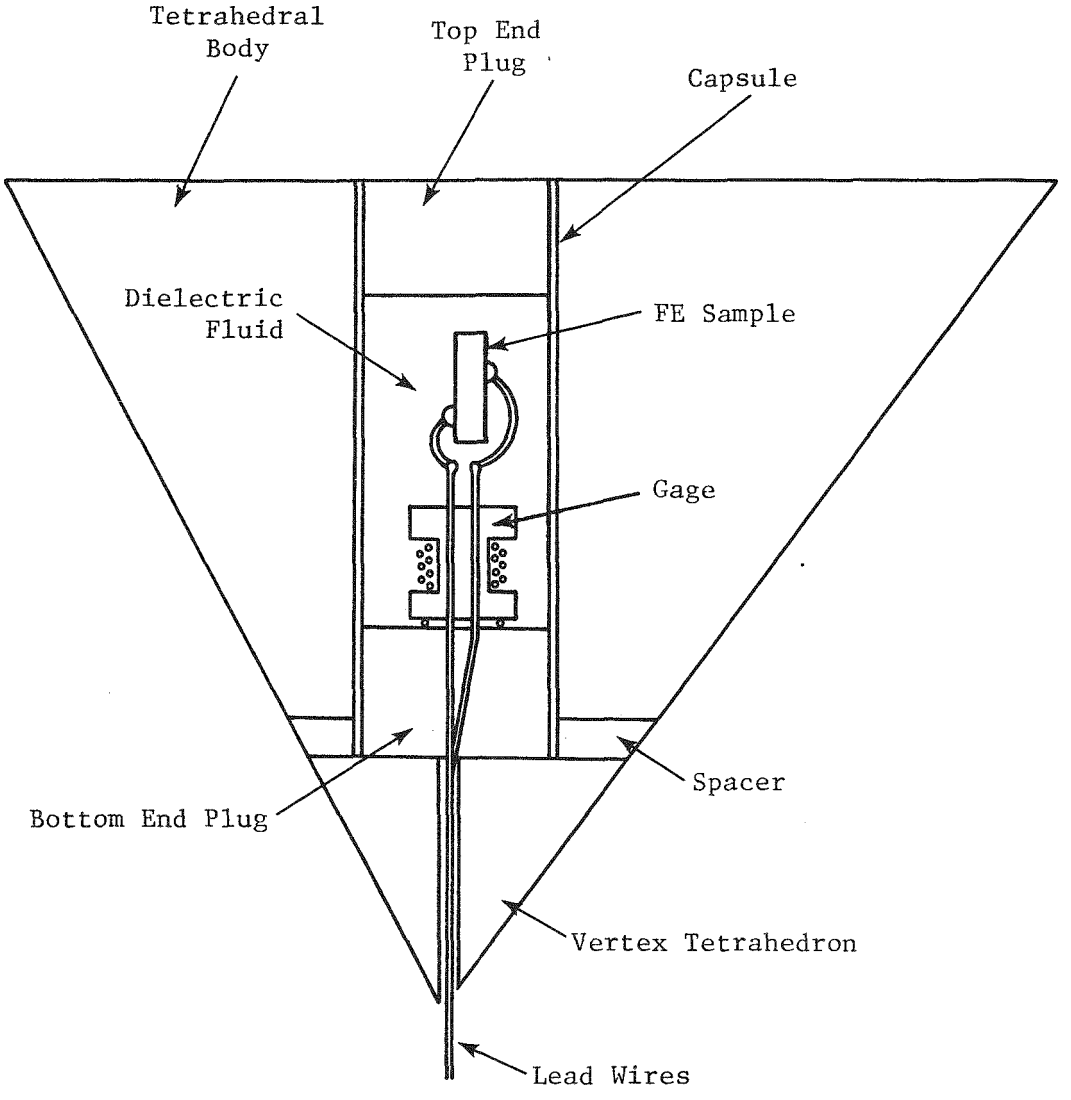

Figure 12. Cross-section of Test Capsule as Positioned in Pyrophyllite Tetrahedron

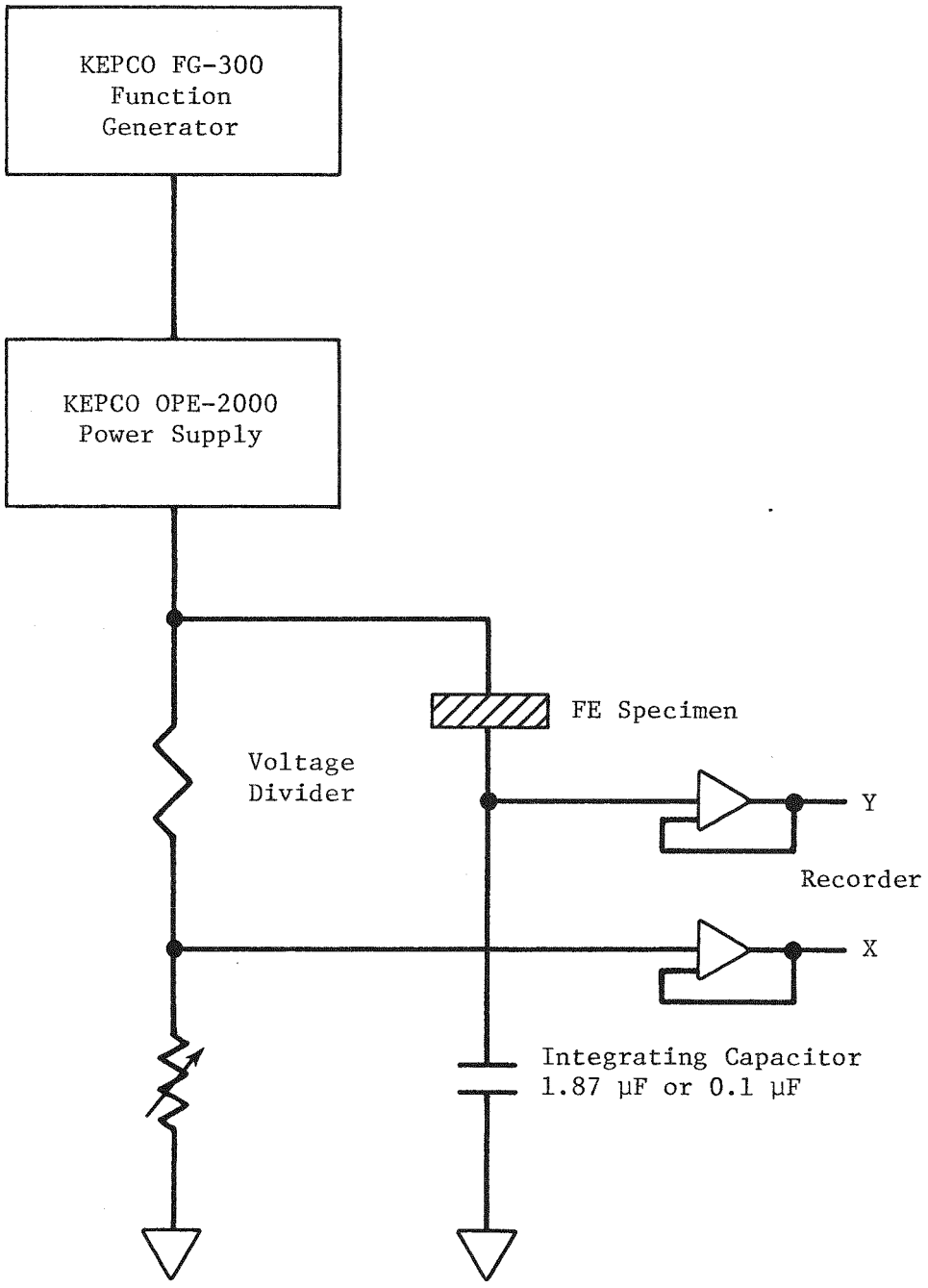

Figure 13. Schematic of Hysteresis Looper Used for Poling and Looping Ferroelectric Specimens

The poling curve was used to measure polarization at high fields. When the ferroelectric was tested below the FE-AFE transition the poling curve was quite "lossy;" thus, the curve was retraced four to five times until the final stabilized curve was obtained. Since the curve is nonlinear, a dielectric constant was arbitrarily determined by measuring the slope from the origin to the point on the curve intersected at an electric potential of 1000 volts.

Dynamic dielectric measurements were made using an HP4270* automatic capacitance bridge. Both capacitance and dissipation factor were determined to four significant places. Frequencies of 1 kHz, 10 kHz, 1000 kHz and 1 MHz were available. The accuracy of this unit is ± 0.1 percent for capacitance and ± 0.1 percent for dissipation factor.

TEST PROCEDURE

Three areas of experimental interest were examined. The first concerned the behavior of PZT 95/5 at the FE-AFE phase change, the second concerned its behavior immediately after the phase change in the nonpolar phase, and the third concerned high pressure dielectric anomalies.

Measurements consisted of initially determining the dynamic capacitance and dissipation factor at the four frequencies available, looping two or more times, poling five or more times, and then repeating the dynamic measurements. This measuring schedule usually took 7 to 10 minutes and continued pressurization of the press was halted during these measurements. There were exceptions to this measuring procedure; in some instances only the capacitance at 1 kHz was measured while the pressure to the sample was slowly increasing or decreasing. Above the FE-AFE transition, looping was usually omitted and only the poling plot was determined.

For measurements relating to the FE-AFE phase transition behavior, the usual pressure change increment between measurements was 50 psi on the Heise gage except near the phase change where the increment size was reduced. At pressures above the FE-AFE phase change the Heise gage pressure increment was usually 250 psi. Where possible, this increment was reduced near the high pressure anomaly.

---

*Trademark, Hewlett-Packard Corp.

DATA ANALYSIS

From hysteresis loops the coercive field and remanent polarization were determined. The coercive field of the loop was calculated by measuring the width of the loop at zero polarization and dividing by two times the sample thickness. Remanent polarization was found by determining the height of the loop (in μC) at zero and dividing by two times the surface area of the sample. Due to the large integrating capacitor used (1.87 μC), it was not necessary to correct for lead wire capacitance.

A typical poling curve is shown in Figure 14. Only the static dielectric constant was determined from the trace; this was specified by the author in an arbitrary fashion. Polarization was taken as the point on the curve where a perpendicular line at 1000 V intersects the lower portion of the tracing. The permittivity was then found by determining $\Delta P/\Delta E$. This value was divided by ε_o to determine the relative dielectric constant. A lead wire correction was made by subtracting a predetermined value of 32 from the calculated dielectric constant. This is the dielectric constant obtained when the lead wires are run without a ferroelectric.

Small signal dielectric constant measurements were made which determined the sample capacitance and dissipation factor. The following lead wire corrections were made to the capacitance value by subtraction: 1 kHz = 1.29 μF; 10 kHz = 1.277 μF; 100 kHz = 1.268 μF; and 1 MHz = 1.260 μF. Only a subtraction of 0.0014 from the 1 MHz dissipation factor was made; the rest were zero. Permittivity was determined by multiplying the capacitance by the thickness and dividing by the area. Relative dielectric constant was calculated by dividing by ε_o. This gave a value of K (or K'). To find K" it was necessary to multiply K' by the dissipation factor as was shown in the section, "Properties of Dielectrics."

During the testing the sample was obviously elastically deformed (and by pore collapse, plastically deformed). The dimensional changes resulting from this deformation were not taken into consideration.

A formal error analysis of the data was not performed. The reason is that the sample-to-sample scatter was considerably larger than any other source of error. Rather than present all data, only typical data which are most representative are shown.

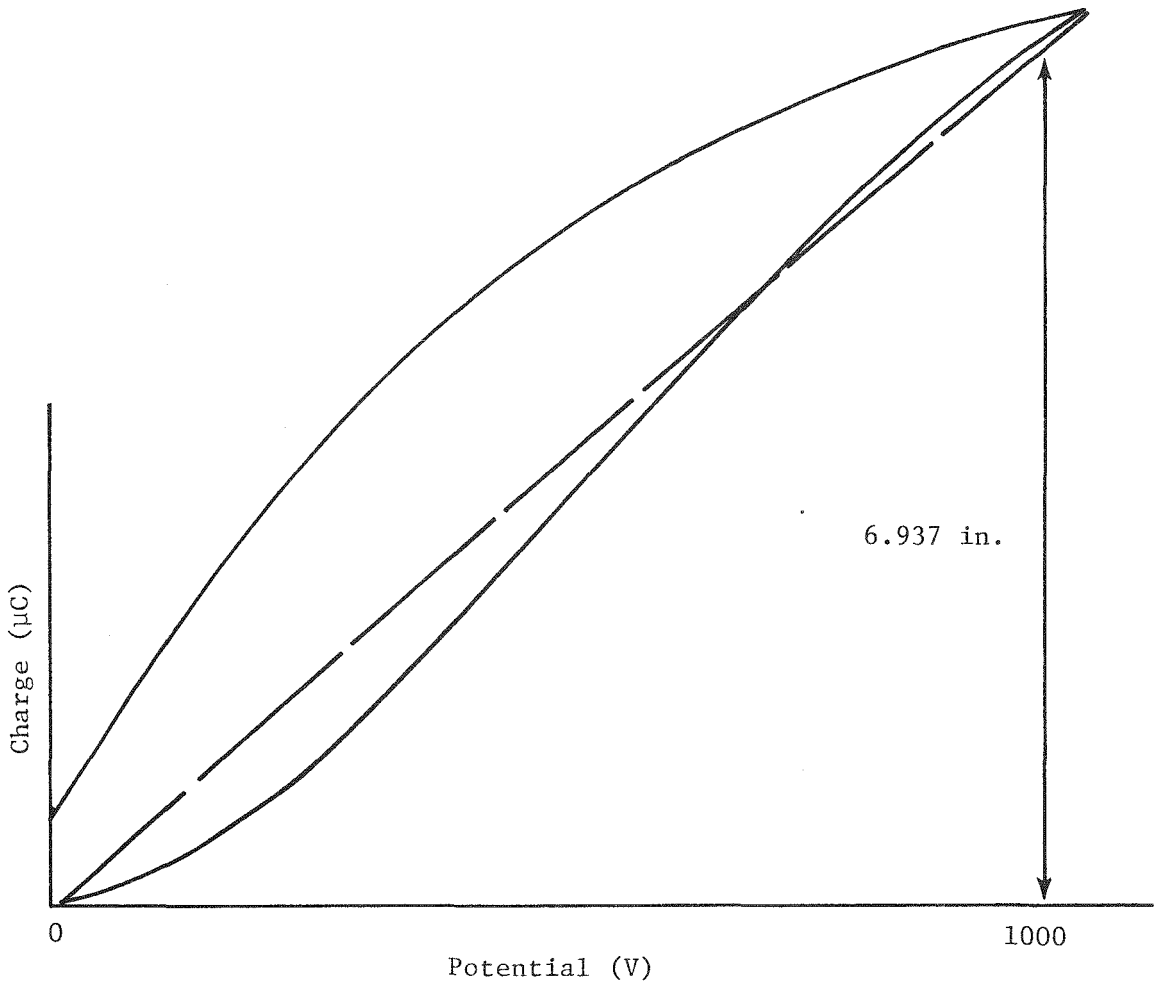

Figure 14. Charge Versus Potential Poling Trace for PZT 95/5 Ferroelectric Ceramic. Dielectric constant measurements were based on the slope from the origin to the curve at 1000 V.

RESULTS

OVERALL RESULTS

Permittivity data for application in depolarization models may take many forms. In the simplified models of Nielson[1] and Anderson,[4] first-order approximations of permittivity in the shocked and unshocked regions as a shock traverses the sample were sufficient. Other models incorporated provisions for pressure dependent permittivity even though high pressure data on most ferroelectric materials had not yet been determined.[5,6,42] The present state of the art has advanced to the point where dielectric relaxation data at each pressure and temperature are desired.[7] This would require a detailed frequency scan of the sample to establish ε_i, ε_s, and the permittivity at frequencies in between ε_i and ε_s. Much of the information in this section may appear to be of academic interest; however, due to the complicated nature of pressure depolarization phenomena, especially in the region behind the shock front where the pressure varies and the electric field may vary, the results should provide a better understanding of the dynamic depolarization process.

Figure 15 is typical of the pressure dependent dielectric behavior (shown as small signal K at 1 kHz versus pressure) of PZT 95/5. In this plot the dielectric constant gradually increases and peaks at the FE-AFE transition; it then abruptly drops and gradually levels off at higher pressures. For the sample shown in Figure 14, hysteresis looping was performed at each measurement interval. For this type of test the average FE-AFE phase transition on six samples occurred at 0.32 ± 0.04 GPa.

It was possible to loop PZT 95/5 at pressures up to the FE-AFE transition. When looping was attempted in the AFE phase, the resulting trace resembled that taken on a "lossy" capacitor. The "lossiness" was greater near the transition than at higher pressures. At pressures immediately following the transition, attempts were made to induce the FE phase by increasing the voltage, but dielectric breakdown occurred.

The initial loop on a typical sample is shown in Figure 16A. Since it had been thermally depoled by heating above the Curie temperature during vacuum drying, 90° as well as 180° domain orientation (as discussed previously) is evident. Figure 16B shows the initial loop on a sample at zero pressure after the sample had been pressure depoled. In this case only 180° domain reorientation is evident. The 180° domain structure is characteristic of the AFE state, so it is possible that the AFE domain structure was retained during depressurization.

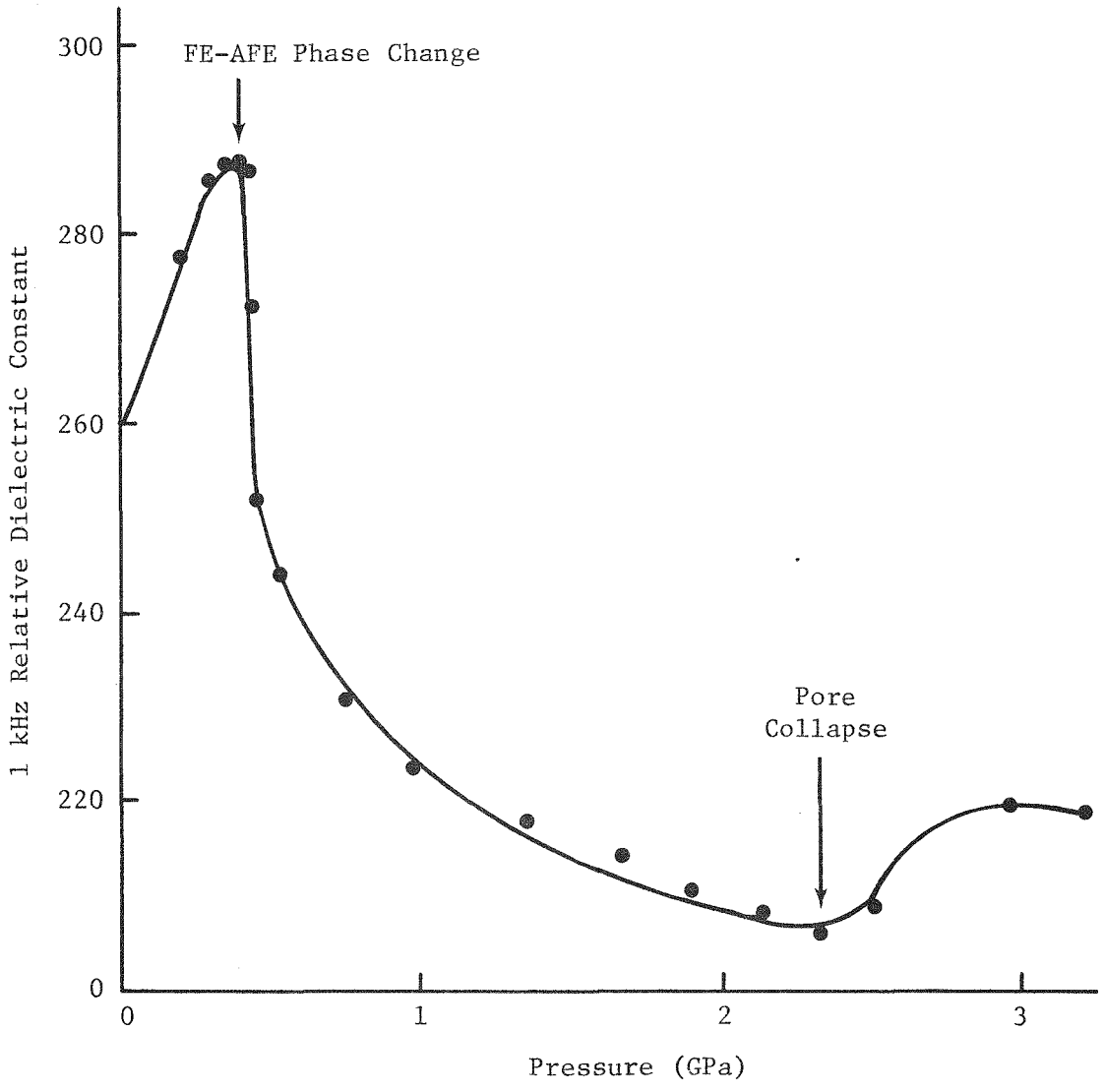

Figure 15. 1 kHz Small Signal Relative Dielectric Constant Versus Pressure for PZT 95/5 Ferroelectric Ceramic

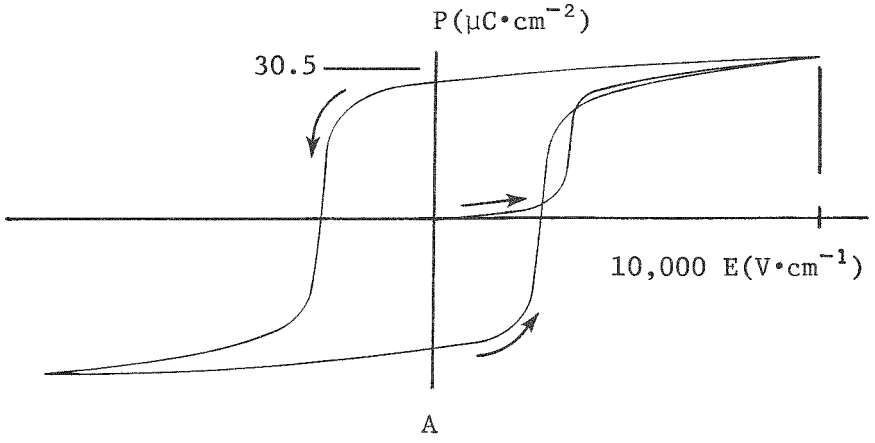

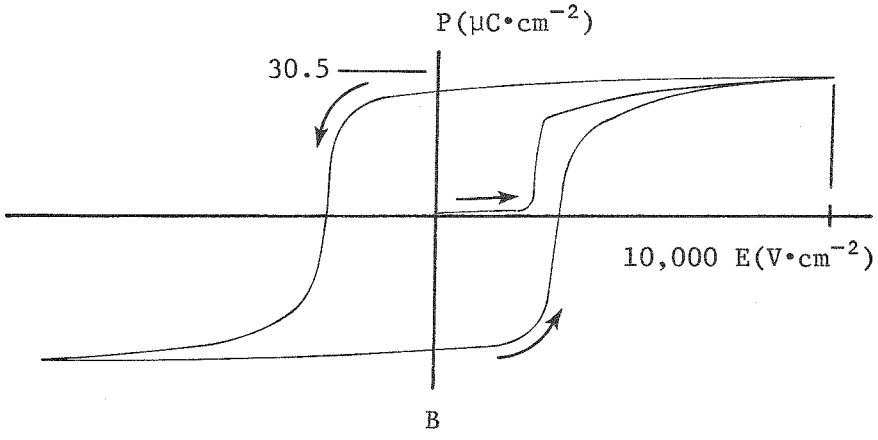

Figure 16. Polarization Versus Electric Field Hysteresis Loop on a Thermally Depoled PZT 95/5 Ferroelectric Ceramic

A. Both 90° and 180° domain reorientation are evident from the initial trace.

B. Predominantly 180° domain reorientation is evident from the initial trace.

The variation of remanent polarization and coercive voltage with pressure up to the transition is shown in Figure 17. It is believed that the remanent polarization discontinuity at the transition pressure is sufficient to verify that the transition is first order.

As mentioned previously, three or more loops were performed at each pressure to assure a stable and repeatable loop. At or near the phase transition, it was possible to induce the non-polar phase by continued looping. The polarization decreased each time the specimen was looped until the nonpolar phase was attained. A series of loops representing this condition is shown in Figure 18.

A graph showing the variation of dielectric constant as measured from the poling trace is shown in Figure 19. At the transition pressure, K increases substantially and the poling trace becomes quite "lossy" as shown in Figure 20. The initial slope of the poling curve is less than that at higher voltages. As a consequence, the small signal relative dielectric constant is lower than the relative dielectric constant shown in Figure 19. After the transition, the difference between these values decreases because the poling traces become less "lossy" at higher pressures.

A dielectric anomaly, which at first was thought to be a phase change, is shown in the high pressure regions of Figures 14 and 19. Based on an average of six runs, the pressure at which this occurred was 2.25 ± 0.15 GPa.

This effect is believed to be associated with pore collapse in the ceramic. Similar results were noted by Polandov et al[39] as mentioned in the High Pressure Static Test Apparatus section. Also (as discussed previously), the two wave patterns noted in shock experiments on ferroelectrics may be associated with this phenomenon.

The effect is irreversible in that it was not encountered during the pressure release cycle or on subsequent pressurization cycles. The sample was too small to determine density changes prior to and after pressurization. Electron microscopy of a sample which had been subjected to pressures above where the effect was noted was attempted but the sample fell apart during polishing and replicating, suggesting that compaction, which caused fragmentation of the specimen, occurred. This fragmentation was also observed on a sample that was retrieved for retest after it had been "compacted." A lead was missing and an attempt was made to re-ball bond another lead in place; however, the sample was easily crushed under the force of the ball bonding anvil.

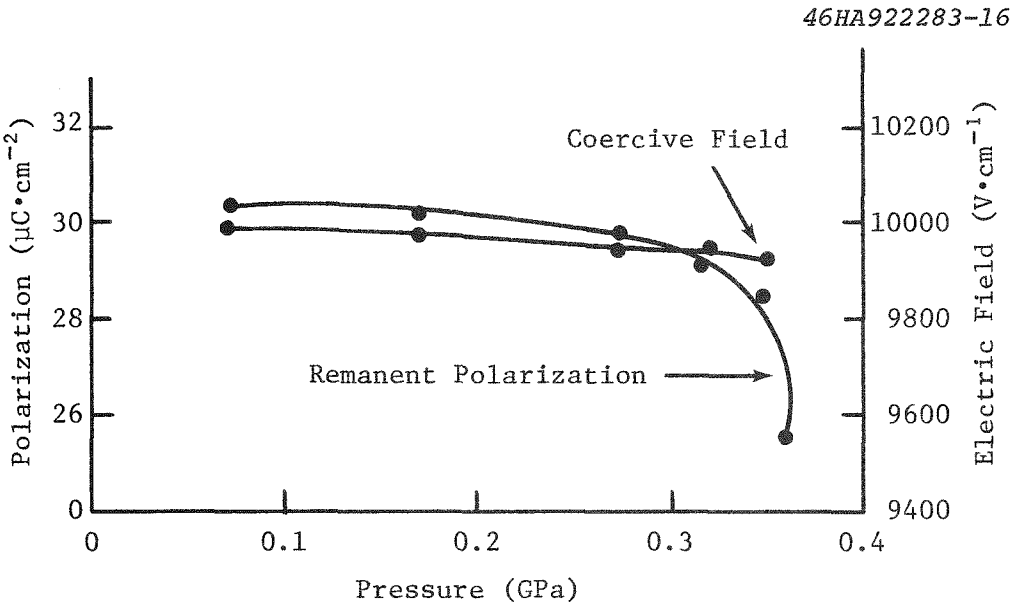

Figure 17. Remanent Polarization and Coercive Voltage Versus Pressure as Measured From Hysteresis Loops on a PZT 95/5 Ferroelectric Ceramic

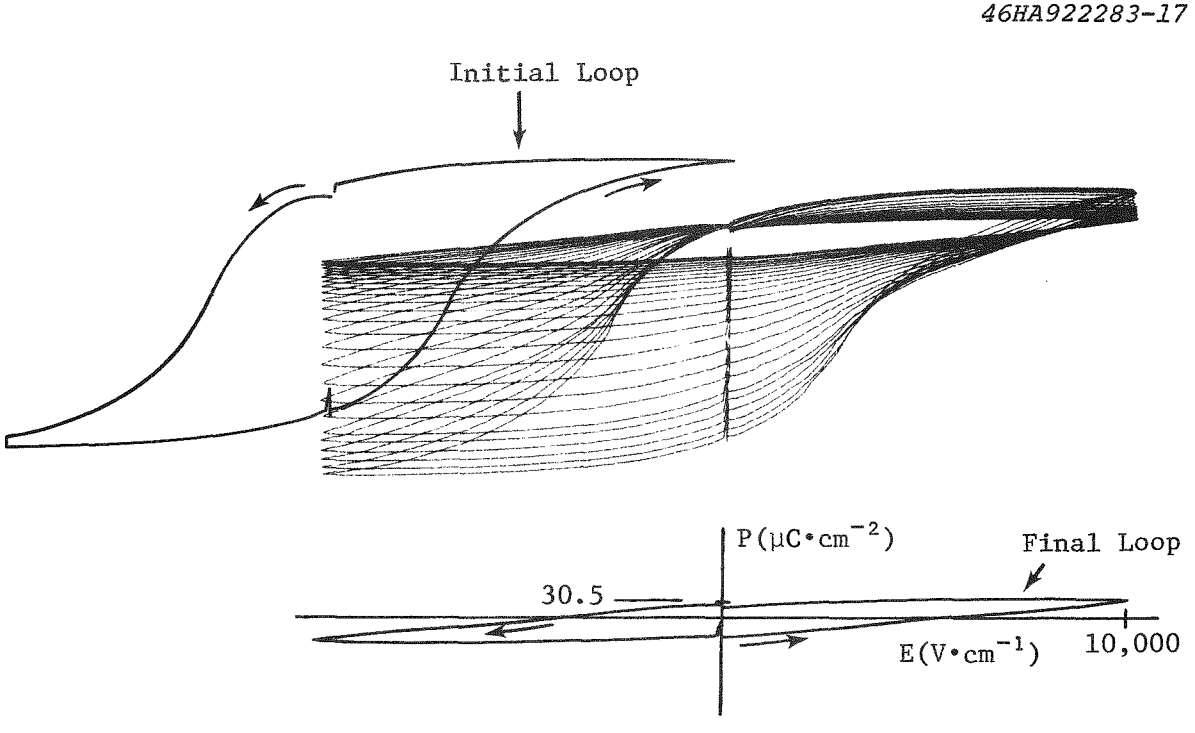

Figure 18. Polarization Versus Voltage Hysteresis Loops Illustrating How Looping Can Induce the AFE Phase at or Near the Transition of a PZT 95/5 Ferroelectric Ceramic

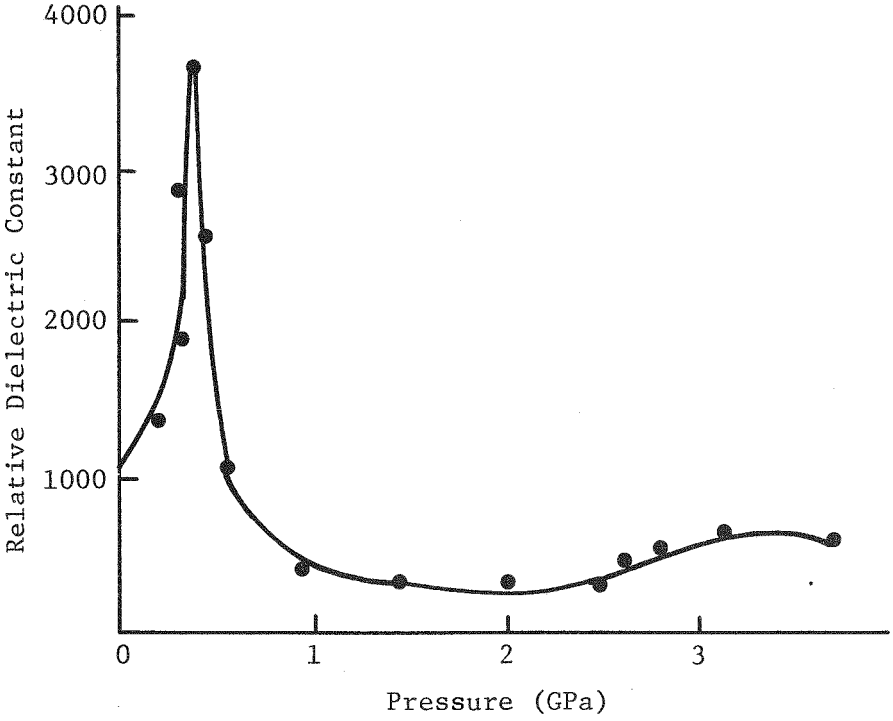

Figure 19. Relative Dielectric Constant Versus Pressure for PZT 95/5 Ferroelectric Ceramic. The dielectric constant was determined by measuring the slope of the poling curve.

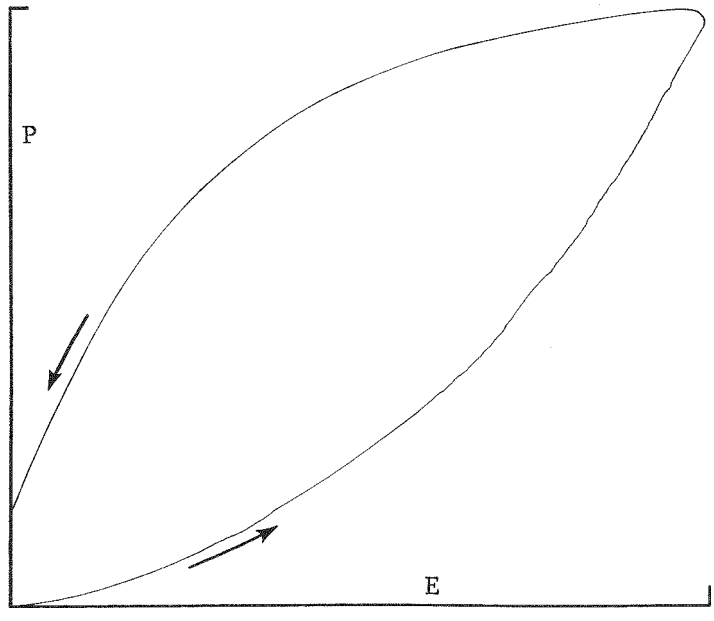

Figure 20. A Typical Polarization Versus Pressure Poling Trace Near the FE-AFE Transition. This curve illustrates the "lossiness" of the sample near the transition.

Loops performed on a compacted sample at zero pressure did not resemble those on a zero pressure noncompacted sample; they appeared like the noncompacted sample loop near the transition region, i.e., similar to the loop shown in Figure 18.

In some cases, the variation in K was sharp and in others it was gradual as shown in Figures 14 and 19. The dielectric constant change that occurred ranged between 10 and 30.

LOW PRESSURE DIELECTRIC CHARACTERISTICS

The small signal dielectric constant at 1 kHz was used to examine a variety of pressurization processes up to and slightly beyond the FE-AFE transition. The initial series of tests consisted of measuring the 1 kHz dielectric constant before and after looping at each pressure interval. The results (Figure 21) show that at each interval up to the transition the dielectric constant increases after looping, while at pressures greater than the transition, the dielectric constant decreases after looping. In Figure 21, it is observed that the dielectric constant varies only slightly between successive pressure intervals which might suggest that there may be only a small change in dielectric constant if the sample were not looped at each pressure interval. However, when K was measured without successive looping it still gradually rose (Figure 22) at a rate that exceeded that of Figure 21. When not looped the phase transition occurred at 0.4 GPa or approximately 0.11 GPa higher than when the sample was looped at each pressure interval. These results, as do those in Figure 18, show that looping provides activation energy that induces a portion of the AFE phase. In so doing, the net dielectric constant is lower as shown in Figure 22, but there is still an increase in K after looping as seen in Figure 21.

The variation of dielectric constant for a sample initially at 0.5 GPa (in the AFE phase) as pressure is released is shown in Figure 23. Looping was not performed at each pressure interval; depressurization was stopped long enough for the pressure to stabilize and a dielectric measurement to be made. When pressure was reapplied (again without looping between each measurement), the curve shown by the dashed line in Figure 23 was followed. From the depressurization curve it is apparent that without looping, the AFE to FE transition is quite sluggish. It is interesting that when pressure is reapplied, a peak in K is encountered at approximately 0.19 GPa.

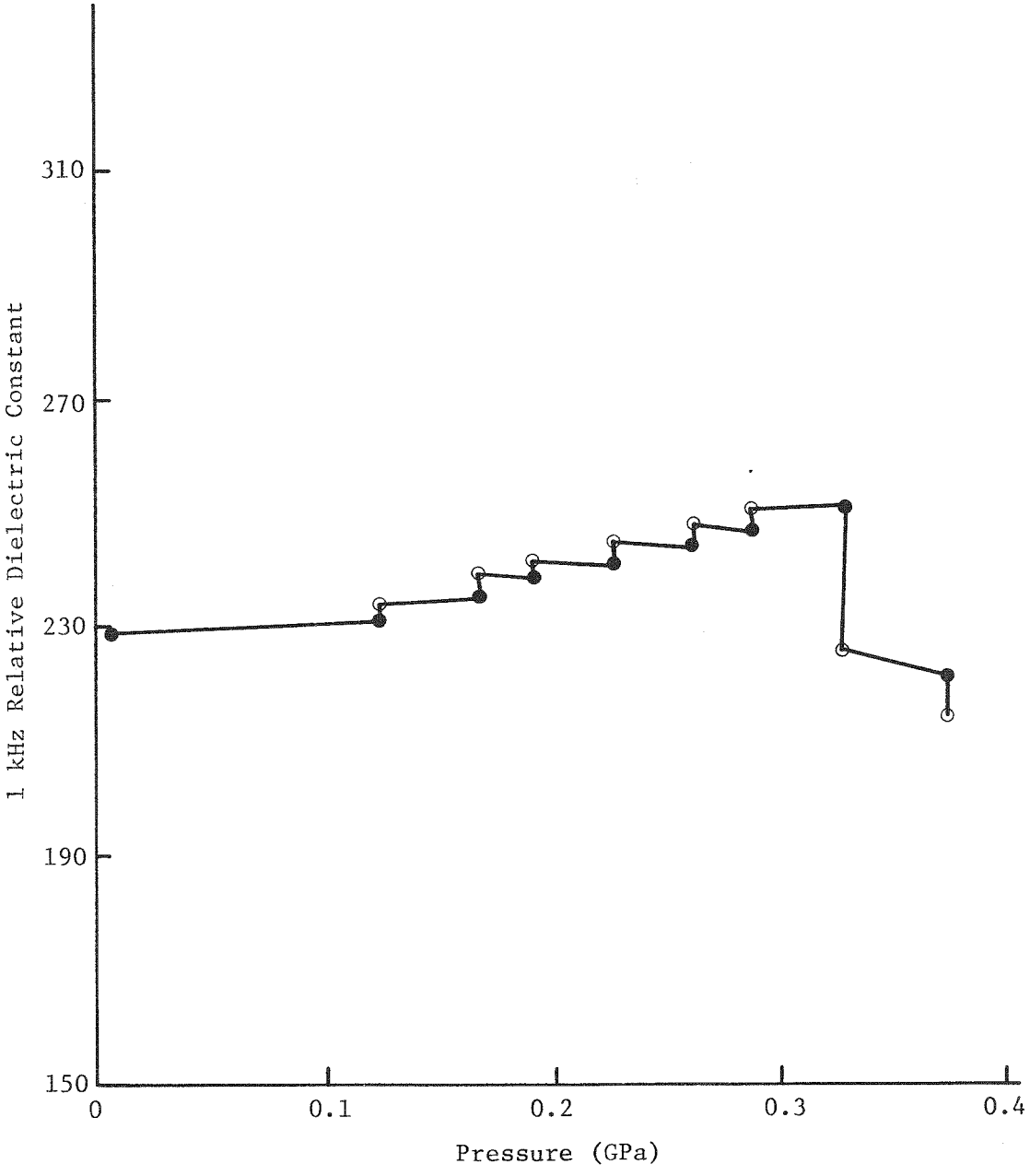

Figure 21. 1 kHz Small Signal Relative Dielectric Versus Pressure for PZT 95/5 Ferroelectric Ceramic. Measurements were made before (solid dots) and after (circles) looping.

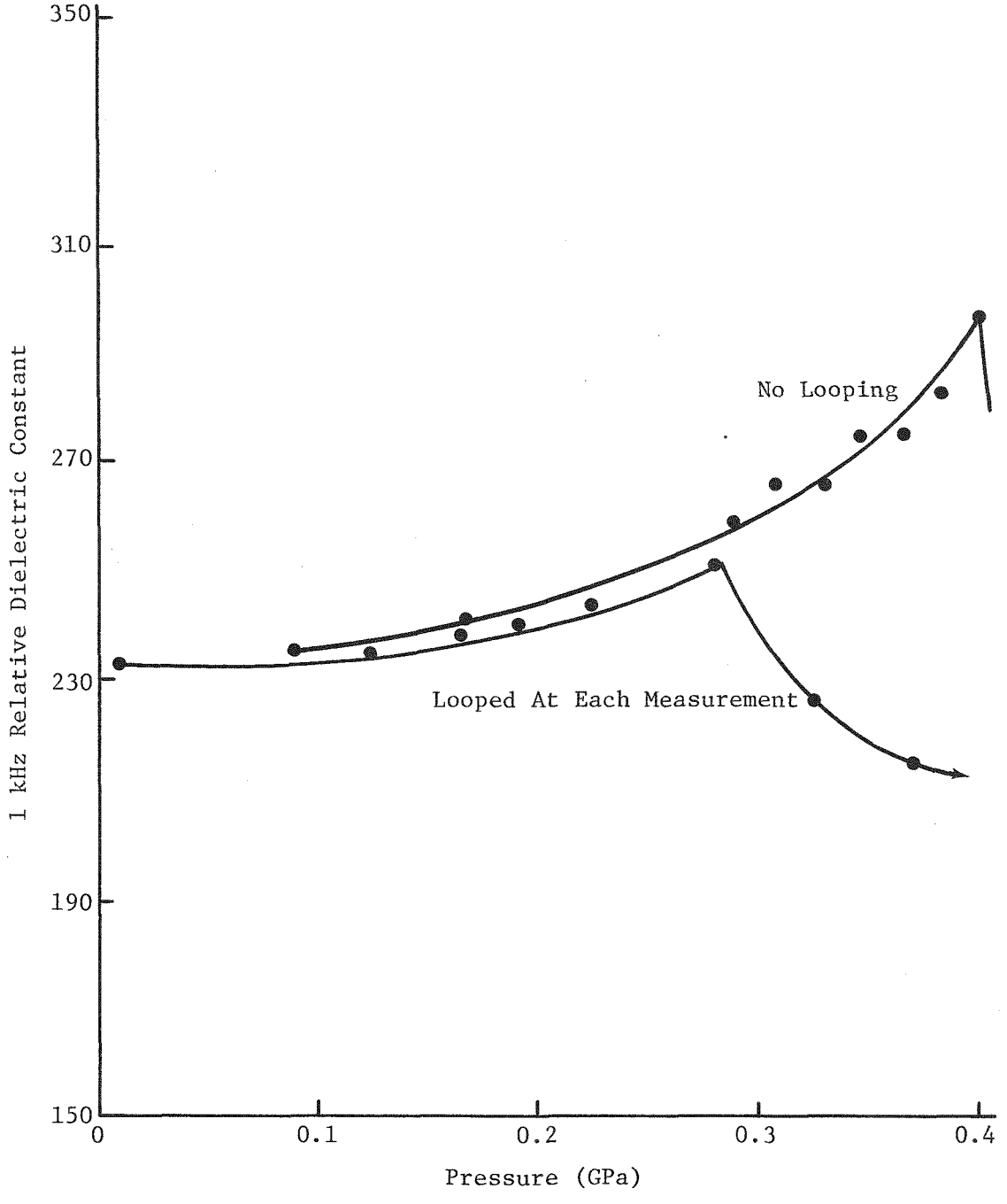

Figure 22. 1 kHz Relative Dielectric Constant Versus Pressure for PZT 95/5 Ferroelectric Ceramic. The lower plot is taken from Figure 21 and shows K when the sample was looped at each measurement. Looping was not performed during the testing for the upper plot.

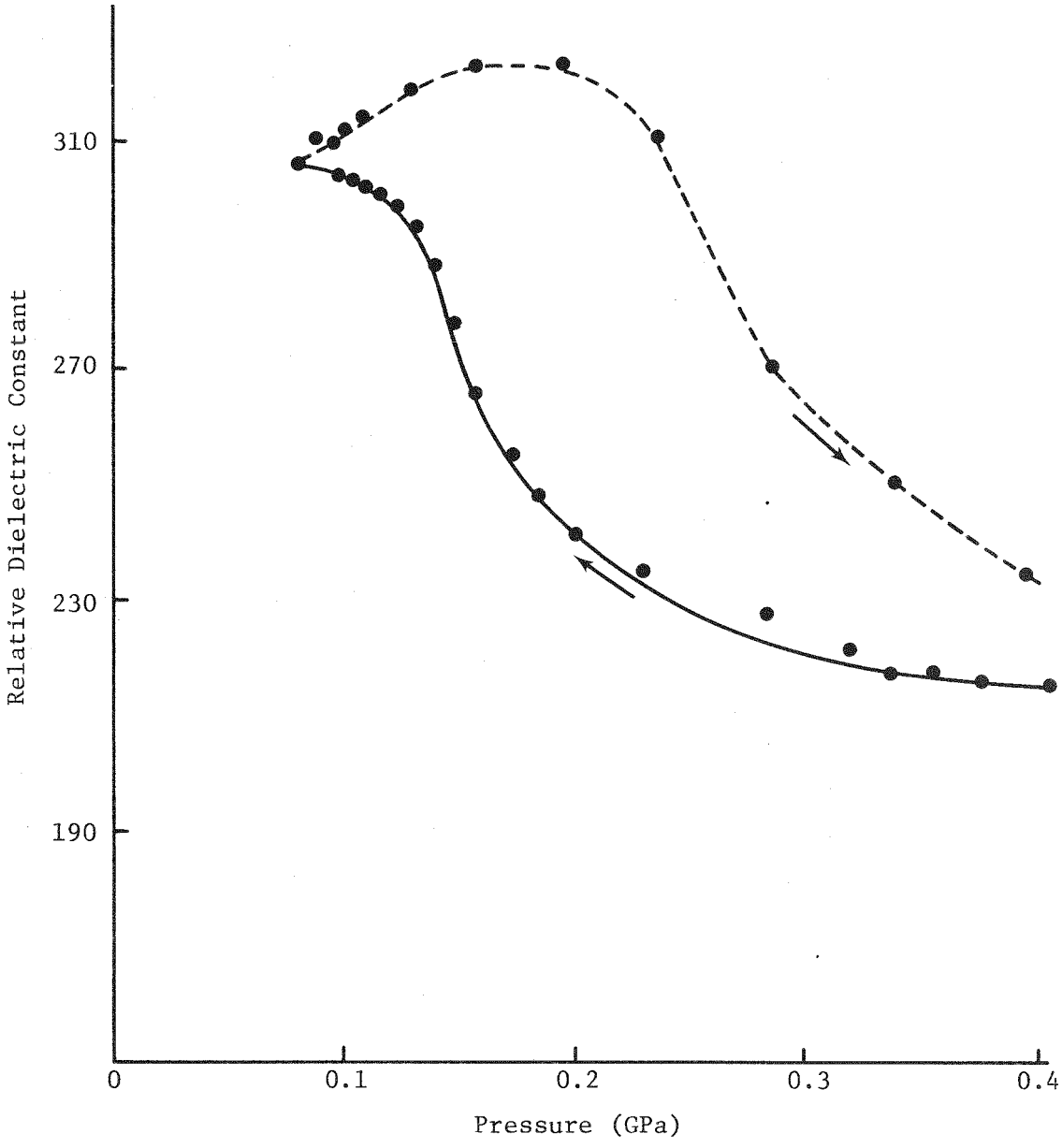

Figure 23. 1 kHz Relative Dielectric Constant Versus Pressure of PZT 95/5 Ferroelectric Ceramic. Testing was initiated when the sample was at 0.5 GPa in the AFE state. The sample was depressurized and repressurized. Looping was not performed between measurements.

Figures 21, 22 and 23 illustrate the dependence of the dielectric response on the degree of polarization. Based on the limited testing that was performed in this sequence, it appears that a model describing the variation of low pressure dielectric properties with electric field may be quite difficult to formulate.

CURIE-WEISS-LIKE BEHAVIOR

In the Ferroelectrics at High Pressure section it was mentioned that at constant temperature the static dielectric constant of $BaTiO_3$, $PbTiO_3$, and $SrTiO_3$ in the nonpolar Fe phase obeys a Curie-Weiss-like relationship. In connection with the present study, it was questioned whether or not PZT 95/5 would follow a similar pattern in the AFE phase. Since the high voltage dielectric characteristics of PZT 95/5 were of greatest interest, practically all of the small signal data were taken prior to or following looping of the sample. As pointed out in the Low Pressure Dielectric Characteristics section, looping at pressures near the transition induces the AFE phase and as a consequence, the small signal dielectric constant is not as large as that determined if looping had not been performed. However, in one run the 1 kHz dielectric constant was measured without intervening looping. Part of the results of this test is shown in Figure 22. The variation of dielectric constant with pressure in the AFE phase is shown in Figure 24. An attempt was made to fit these data to a Curie-Weiss-like relationship similar to the method used by Samara[33] in fitting $BaTiO_3$ data.

By extrapolation of 1/K to zero when plotted against p, it is possible to find p_o. This was determined to be 0.34 GPa (Figure 24). With this value, a plot of K versus $1/(p-p_o)$ was constructed. The results (Figure 25) indicate that the relationship is linear; however, instead of fitting a single term Curie-Weiss-like equation, an additional term corresponding to the y intercept was necessary. For this sample, the resulting Curie-Weiss-like relationship was found to be

$$K = 187 + 55/(p - p_o) \qquad (14)$$

In the nonpolar PE phase, Samara[11,33,34,35] was able to demonstrate an excellent fit of the data to a single term equation. The test procedure and compositions resulted in a much greater increase in dielectric constant at the transition than was determined in the present study. If a smaller pressure interval had been selected between measurements, a larger dielectric constant peak at the transition (and thus greater accuracy) would have resulted. Another difference was that Samara examined the static dielectric constant while this study used the 1 kHz relative dielectric constant. As will be shown in the next section, the two values are nearly the same in this pressure range.

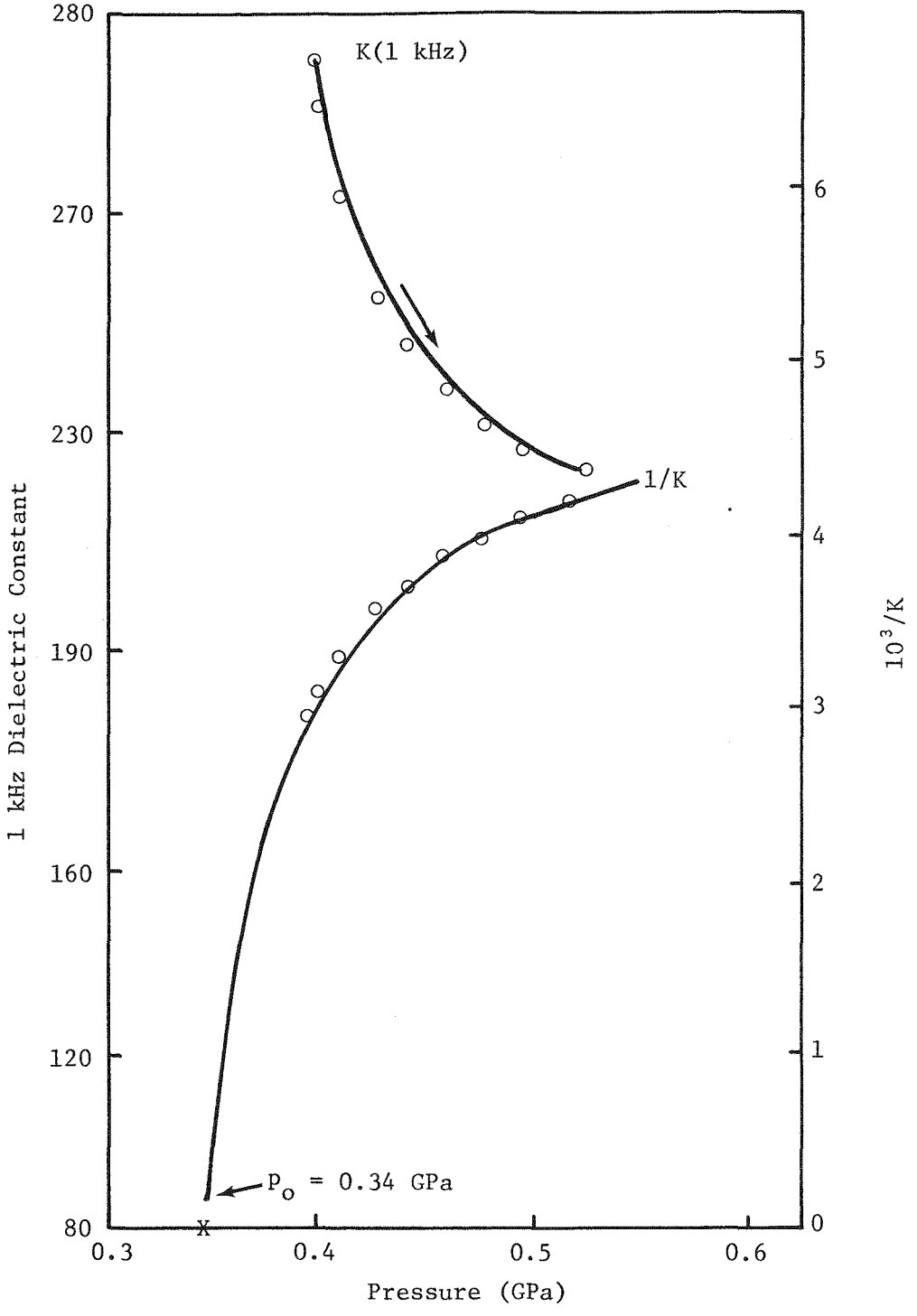

Figure 24. Pressure Versus 1 kHz Dielectric Constant in the AFE Phase for PZT 95/5 Ceramic. The reciprocal dielectric constant is plotted to determine p_o.

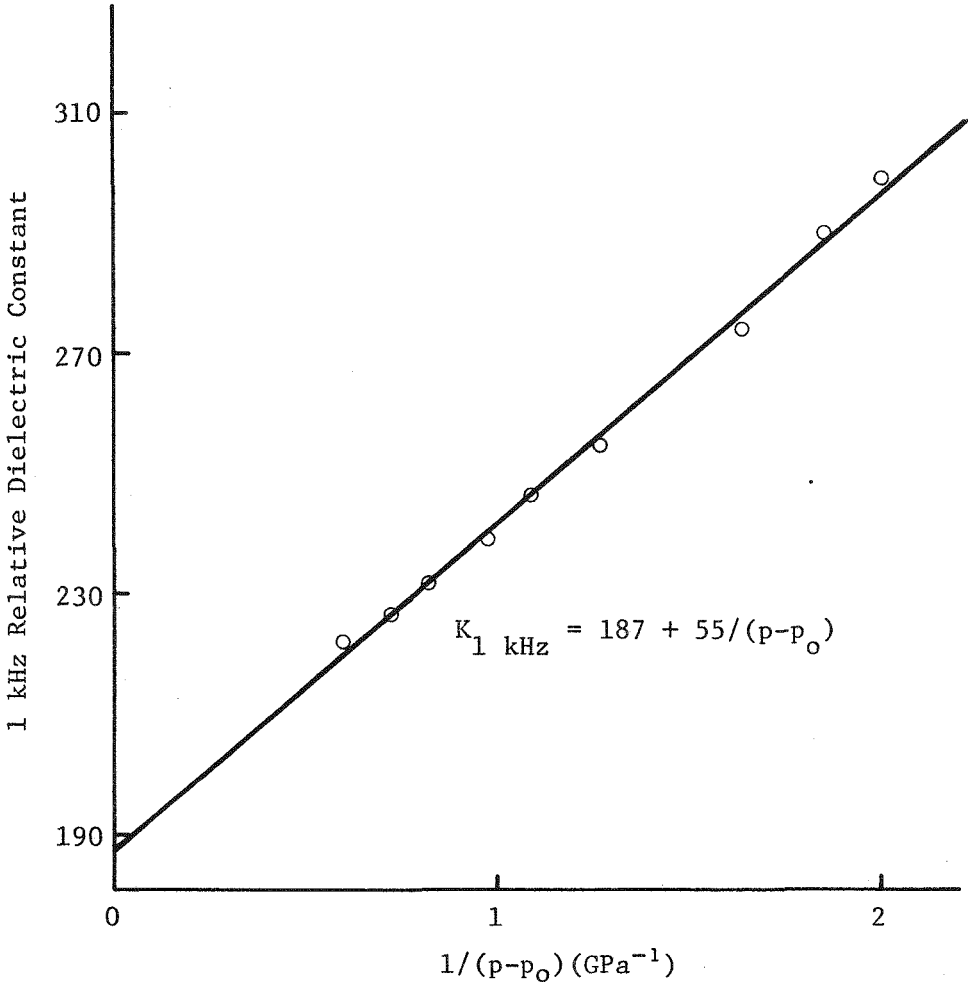

Figure 25. 1 kHz Relative Dielectric Constant Versus $1/(p-p_o)$ Demonstrating That a Curie-Weiss-Like Relationship is Followed for This Ceramic in the AFE Phase. For these calculations p_o = 0.34 GPa. The resulting relationship is shown on the illustration.

It was of interest to examine data in which looping (or poling) was performed at each measurement interval. Figure 26 is a graph of three tests in which 1/K versus pressure was plotted to determine p_o. It is seen from the extrapolation of data from test run No. 8 that p_o could encompass a range of values. Graphs of dielectric constant versus $1/(p-p_o)$ for values of p_o ranging from -0.4 to 0.2 GPa are shown in Figure 27. A linear fit of the data appears to be possible at pressures near the transition but deviates at higher pressures. For this sample, as p_o decreases, linearity increases. It is evident that Curie-Weiss-like relationships are quite dependent on p_o; thus, it is mandatory that care be exercised in gathering experimental data about the transition so that the peak value of dielectric constant can be determined. This would increase the accuracy with which p_o could be determined.

FREQUENCY DEPENDENT BEHAVIOR

As mentioned previously, small signal measurements consisted of determining the dielectric constant and dissipation factor at 1 kHz, 10 kHz, 100 kHz and 1 MHz. With these data, it is possible to determine the imaginary components of the complex dielectric constant at various frequencies and if a sufficiently wide range of frequency is available, dielectric relaxation characteristics can be determined. Table 1 is a listing of the complex dielectric constant components of PZT 95/5 determined on a typical pressurization run. For conciseness only a part of the results is shown in the table.

At a particular pressure, the components of the complex dielectric constant were determined (as explained in the Properties of Dielectrics section) and plotted on a complex plane. Figure 28 shows graphical representations of K' and K'' at selected pressures. The plots at 0.089 and 0.384 GPa represent the dielectric character of a poled ferroelectric below the transition. The concave upward curvature does not resemble any of the common relaxation models described previously although the data may fit some of the other models described in reference 8. After the FE-AFE transition, the curvature is such that if extrapolated to the real axis it would be possible to obtain the static dielectric constant, K_s. After the pressure is increased past 1.64 GPa, the curve becomes concave downward and resembles the distributive relaxation time model described in the Properties of Dielectrics section.

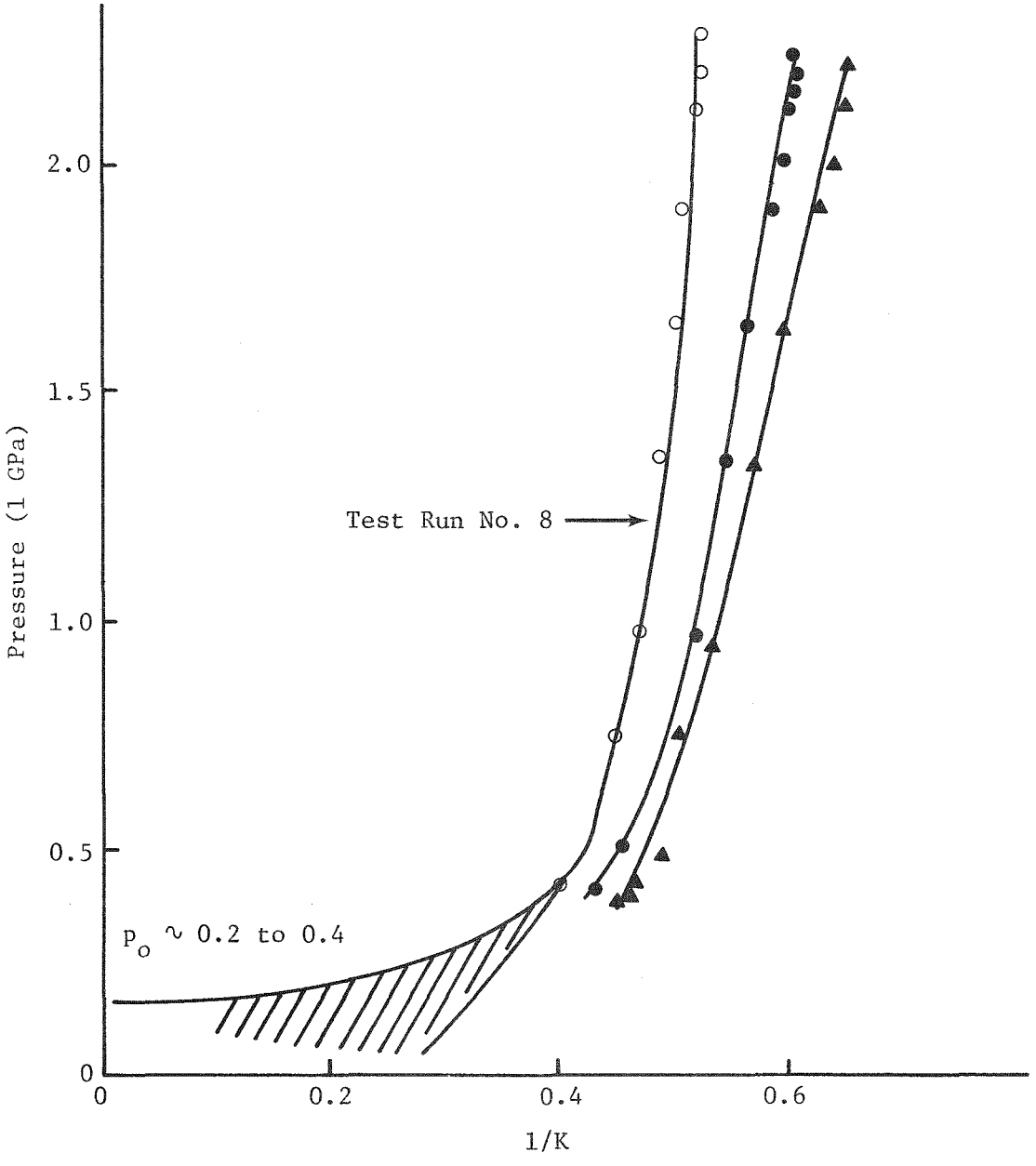

Figure 26. Pressure Versus the Reciprocal of the 1 kHz Relative Dielectric Constant for High Pressure Examinations of Three PZT 95/5 Ceramic Samples. The samples were looped between each measurement.

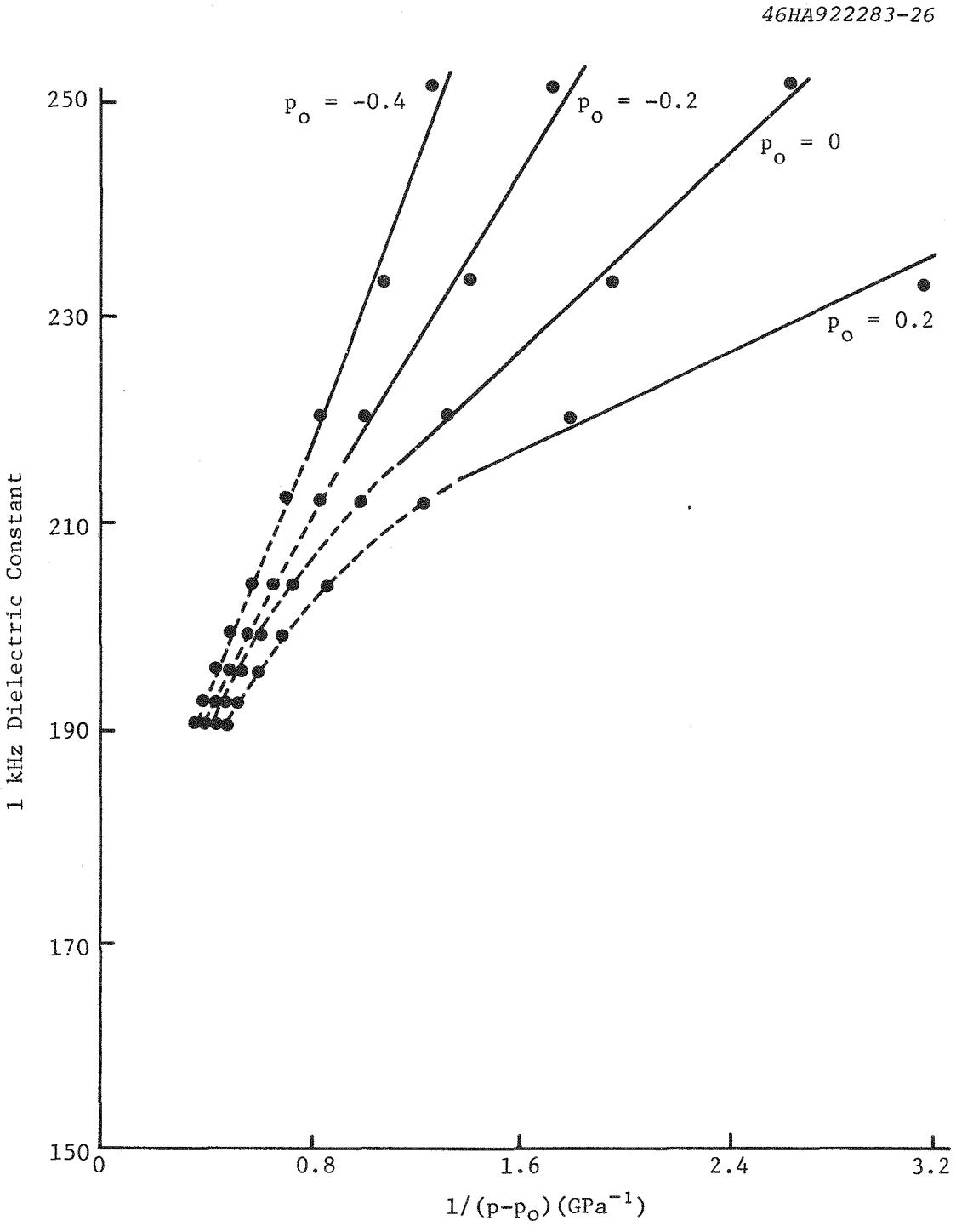

Figure 27. 1 kHz Relative Dielectric Constant Versus $1/(p-p_o)$ for PZT 95/5 Ceramic. Four values of p_o were examined in conjunction with the data from test run 8 in Figure 26 to determine how p_o affected linearity.

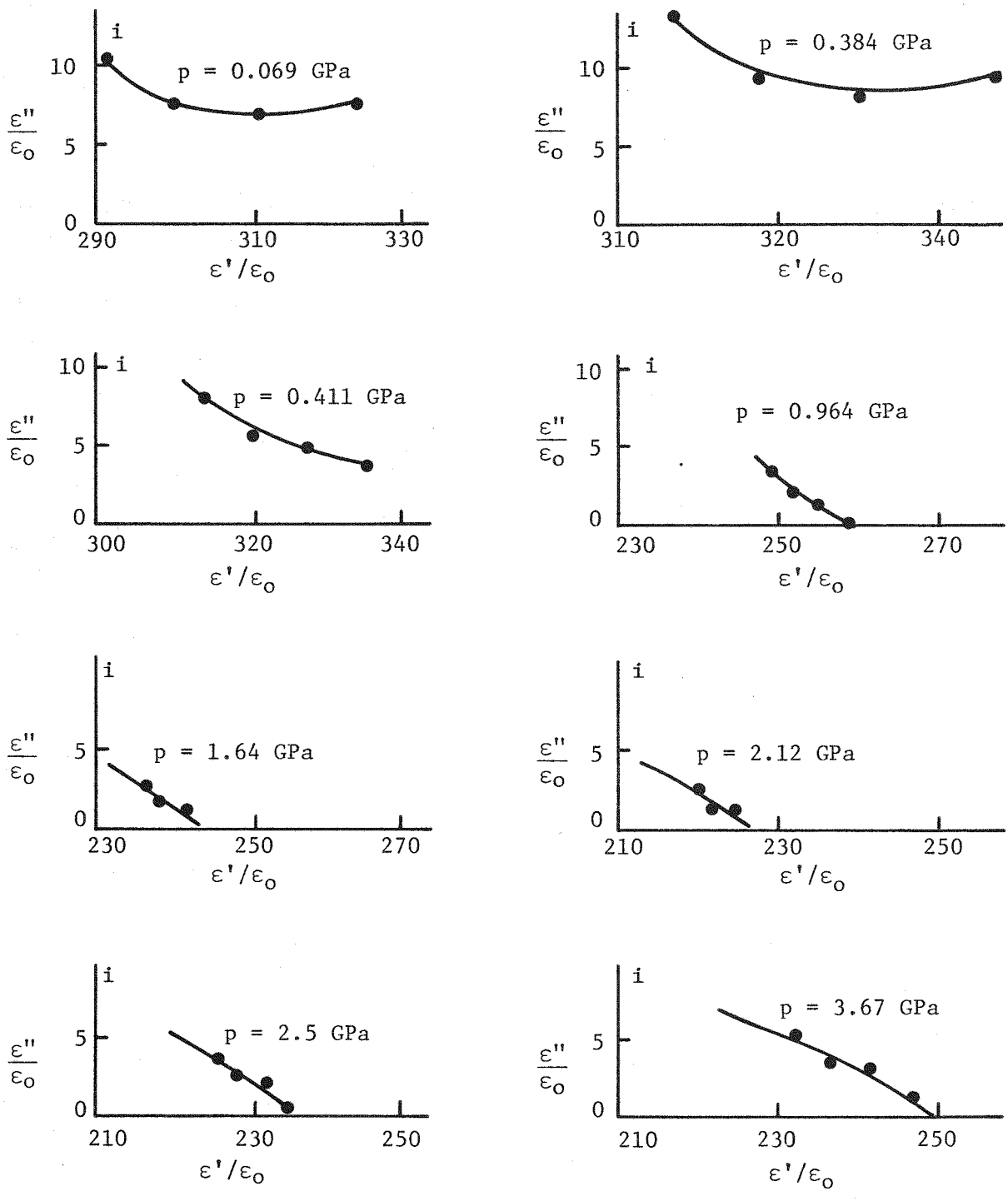

Figure 28. Components of Complex Dielectric Constant (K' and K'') Plotted on Complex Plane at Various Pressures. The static dielectric constant K_s is location at which plot extrapolates to real axis.

Table 1. Real and Imaginary Complex Dielectric Constant Components of PZT 95/5 Ferroelectric Ceramic When Tested at Four Test Frequencies at Pressure up to 3.67 GPa

Pressure (GPa)	Relative Dielectric Constant at Specified Frequency							
	1 kHz		10 kHz		100 kHz		1 MHz	
	$\varepsilon'/\varepsilon_o$	$\varepsilon''/\varepsilon_o$	$\varepsilon'/\varepsilon_o$	$\varepsilon''/\varepsilon_o$	$\varepsilon'/\varepsilon_o$	$\varepsilon''/\varepsilon_o$	$\varepsilon'/\varepsilon_o$	$\varepsilon''/\varepsilon_o$
0.069	322	7.56	309	7.12	299	7.56	291	10.2
0.302	355	9.19	338	8.76	325	9.21	315	12.7
0.384	358	9.55	341	8.95	328	9.42	317	13.2
0.411	334	3.73	326	4.86	319	5.30	313	7.02
0.506	289	1.82	284	3.32	279	3.69	275	5.07
0.964	257	0.616	254	1.28	251	2.31	250	3.62
1.64	242	0.096	241	1.74	237	1.94	236	2.80
2.12	226	0.0	224	1.52	222	1.77	220	2.53
2.50	234	0.91	231	2.38	227	2.64	225	3.71
2.95	251	1.93	246	3.57	241	3.95	236	5.06
3.67	248	1.78	243	3.52	238	3.90	233	5.19

From the data used to construct Figure 28 at pressures of 1.64 GPa and above, it may be possible to determine the instantaneous dielectric constant, K_i, if the distributive relaxation time model is assumed. After an examination of this possibility it was decided not to continue for the present study. The reason is due to the fact that it is felt that the resulting value of K_i would contain such a large degree of uncertainty that it would not be of any value and would possibly be misleading in shock depolarization studies. It is felt that to obtain this information, additional testing in a higher frequency range should be performed.

SUMMARY AND CONCLUSIONS

Electrical measurements pertinent to the dielectric characterization of PZT 95/5 ferroelectric ceramic were determined as a function of pressure up to 4 GPa. A 600/2400 tetrahedral anvil apparatus was used to attain the pressures desired. This required development of a test fixture which could subject the specimen to truly hydrostatic pressures and high voltages. An accurate measurement of the pressure was made using a Manganin wire pressure transducer.

The purpose of the study was to establish dielectrical data which could be applied to shock depolarization models. Low signal dielectric constant results as well as high voltage poling dielectric results were determined as a function of pressure. These data have direct application to some of the simpler shock depolarization models. More refined models require knowledge of the dispersion and relaxation characteristics of the dielectric. Specifically, it is desired that the dielectric constant be specified over a frequency range between the static and instantaneous dielectric constant. It was found that at high pressures when the components of the complex dielectric constant were plotted, the data resembled a distributive relaxation time model near the static dielectric constant. However, it is not feasible to calculate an instantaneous dielectric constant because of the large extrapolation error. To obtain these data, an investigation at higher frequencies is needed.

Based on small signal dielectric measurements with no looping, the FE-AFE transition was located at 0.4 GPa. When the sample was looped at each pressurization interval, the transition pressure was lower (it averaged 0.32 GPa). The electric field induces and stabilizes a portion of the AFE state while the material is considered to be in the FE phase.

Due to the fact that one of the intentions of this program was to establish high voltage characteristics of PZT 95/5 with pressure, only one test was scheduled where only small signal data with no intervening looping was performed. For this single test, data in the AFE phase immediately following the transition were found to fit a Curie-Weiss-like relationship.

An anomaly at high pressure was observed. This was thought to be a phase change but due to the fact that it was irreversible as well as the fact that the material was easily fragmented, it is concluded that the effect is attributed to collapse of pores in the ceramic. Similar results were reported by Russian experimenters.[39]

Except for a study by Berlincourt and Krueger[22], which examined low signal dielectric properties of PZT 95/5 up to 0.5 GPa, to the author's knowledge the present work represents the only study of PZT 95/5 at high voltages and high static pressures. It is believed that the data will contribute to the understanding of shock depolarization modeling and to the understanding of PZT 95/5 at high pressures.

APPENDIX A

TETRAHEDRAL PRESS DESCRIPTION AND OPERATION

For the 600/2400 tetrahedral anvil apparatus used in this study, the rams were made up of an anvil assembly mounted on a 30.5 cm diameter piston. The anvil consisted of a 4.76-cm diameter cemented tungsten carbide cylinder having an equilateral triangular face with an edge length of 3.18 cm.

A diaphragm air pump in the control console was used to pressurize the hydraulic oil which in turn drove the rams. Mounted on the control console was a zero to 1100-psi Heise gage that indicated the hydraulic oil pressure. The face of this gage was incremented in 100-psi intervals and was readable to the nearest 10 to 15 psi.

The operation of the presses of this nature is not complex. The most critical item concerns the initial adjustments of the drawback mechanisms and the pressure release cycle which, if performed too rapidly, results in a specimen "blowout." With the tetrahedral press, once pressure is applied, the operator has little control except for the rate of pressurization. A schematic of the pressurization system is shown in Figure A-1.

On the back side of the platens of these presses are hand-operated devices called drawback mechanisms which retract the rams once they have been extended. To aid in ram retraction, the intake line of a vacuum pump was plumbed into the top of the oil reservoir. A partial vacuum on the hydraulic oil would draw oil from the four cylinder cavities and retract the rams. In like fashion, to extend the pistons, the oil reservoir was pressurized to as much as 200 kPa with air. These adaptions eliminated a large part of the effort and time required to manipulate the drawback mechanisms.

The steps taken in the initial adjustment of the anvils as well as the steps taken to operate the press are outlined below. Preliminary procedures describing how the rams are retracted and advanced are given.

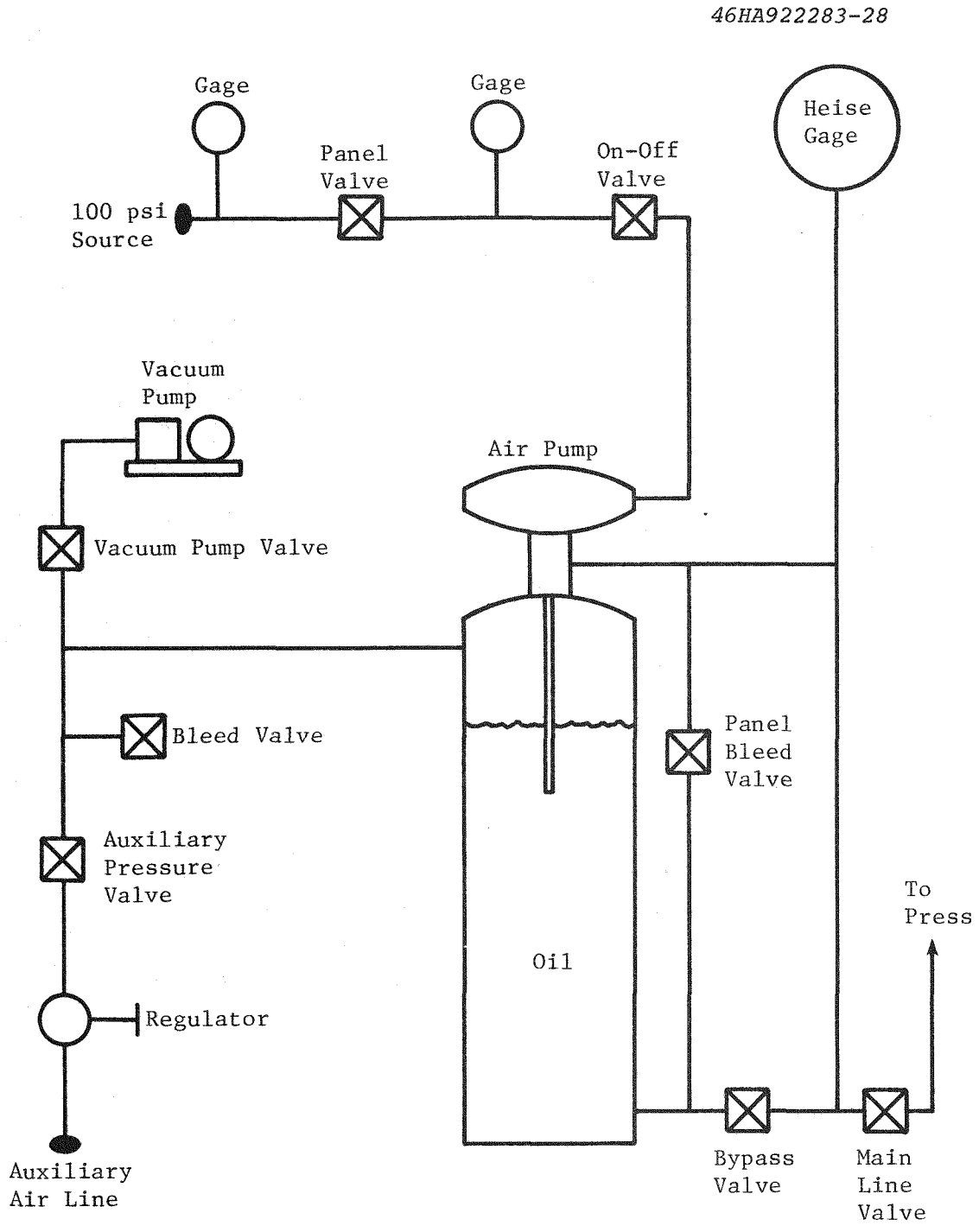

Figure A-1. Schematic of Tetrahedral Anvil Apparatus Pressurization System

Advancement of Rams (Figure A-1)

1. Close vacuum pump valve.

2. Open auxiliary pressure line valve, main line valve, bypass valve, and panel valve.

3. Adjust drawback mechanism.

4. Adjust regulator on auxiliary pressure line to 15 to 30 psig depending on ram advance rate desired. (The ram advancement can be stopped at any position by adjustment of the drawback mechanisms.)

Retraction of Rams (Figure A-1)

1. Close auxiliary pressure line valve.

2. Open vacuum pump valve, main line valve, bypass valve, and panel valve.

3. Adjust drawback mechanism.

4. Start vacuum pump. (Ram retraction can be stopped at any position by adjustment of the drawback mechanism.)

Alignment of Anvils (Figure A-1)

1. With top platen removed, adjust each lower ram until piston face is flush with platen face.

2. Advance rams until the three anvils are close to touching. (It is desired that rams can be positioned such that anvil edges when touching will form a "nest".)

3. Adjust the anvil assembly position by rotating the two eccentric adjusting rings between the anvil assembly and piston. (By making these adjustments and advancing or retracting the rams, it is possible to form the nest.)

4. Retract rams and align piston faces flush with platens.

5. Advance rams until the nest is formed. Note the exact number of turns on the drawback mechanisms required to form the nest. (For the present study the turns were 18 for No. 1 ram, 11 for No. 2 ram, and 7 for No. 3 ram.)

6. Position top platen and replace hinge pins. Connect ram No. 4 hydraulic line. To accomplish this it may be necessary to retract the rams of the lower platens.

7. Advance lower rams to form nest (if not already). Lower top ram and adjust anvil assembly using eccentric adjusting rings. By careful adjustments it is possible to close the tetrahedral nest. (Visual access is limited; thus, an indirect method such as attempting to hold the gap between the anvil binding rings uniform can be used as a possible alignment method.)

Pressurization Cycle (Figure A-1)

1. Position pistons of lower rams flush with platen faces.

2. Place pyrophyllite tetrahedron in press. (The top ram should be withdrawn sufficiently from the previous run to allow the tetrahedron to slip into place.)

3. Support tetrahedron so that it is not locked in place by the lower anvils. (For this study the support consisted of a 3.1-mm diameter copper wire bent into a U-shape approximately 50 cm on a side.)

4. Adjust drawback mechanisms of the lower rams so that when extended they will be within two or three turns of nest position.

5. Adjust air regulator of auxiliary pressure to 25 to 30 psig.

6. When two of the three drawback mechanisms tighten, remove tetrahedron support mechanism and advance the top ram. Check to be sure electrical leads are properly located and not wedged between two anvils.

7. When drawback mechanisms on all lower platens are tight and the top anvil is close to the tetrahedron, reduce regulator pressure of auxiliary air to 10 psi. (Additional adjustments of the drawback mechanisms of the lower rams may be required.)

8. When the top anvil contacts specimen, reverse drawback mechanism until tight. (Anvil-tetrahedron contact for the top ram is difficult to determine. The present study relied on operator judgment of the gap between binding rings. The possibility of using a thin wire between the tetrahedron and anvil was examined, i.e., anvil closure occurred when the wire was wedged. Too much force by the top anvil at this stage is detrimental because it will cause the lower anvils to retract.)

9. Immediately turn auxiliary air supply off and bleed to atmosphere.

10. Tighten bypass valve and panel valve.

11. Check test sample instrumentation.

12. Start press air pump and pressurize until Heise gage reads 10 to 20 psi.

13. Advance all drawback mechanisms 10 turns.

14. Place protection covers in place.

15. Continue pressing.

Depressurization Cycle (Figure A-1)

1. If at high pressure (over 1000 psi on the Heise), slowly lower pressure using panel valve. (For these tests it was found that a 100-psi drop in 20 seconds was a sufficiently slow rate to prevent specimen blowout.)

2. When at (or close to) zero psi on the Heise gage, remove protection covers and retract rams.

3. By adjusting drawback mechanisms, stop rams of lower platens when each piston face is flush with platen face. (It is possible to accomplish this without operator attention by proper adjustment of drawback mechanisms. For this study it was found that by advancing the No. 1, No. 2, and No. 3 drawback mechanisms 3, 4, and 11 revolutions, the rams would withdraw to the correct position.)

4. The top ram should be retracted more than just the amount required to remove the pressed tetrahedron; space should be allowed to fit the tetrahedron for the next test. (For this study the extraction of the tetrahedron was performed using a 50-cm long, 3.2-mm diameter steel wire having a 90° bend at one end with a 3-cm leg.)

5. Turn vacuum pump off.

APPENDIX B

FABRICATION OF TETRAHEDRON

The pyrophyllite used for these studies was in the form of 30.6-cm long prisms having a triangular cross-section. Two legs of the triangle were 4.4-cm long while the other was 5.2 cm. Each prism was cut into 6 equal pieces by sectioning perpendicular to the axis at 5-cm intervals. Using Crystalbond 509* thermoplastic cement, which flows at approximately 135°C, a 1.5-cm diameter by 6-cm long steel rod was bonded to the largest rectangular face of each piece as shown in Figure B-1.

This assembly was then placed in an indexing tool mounted at the appropriate angle on the bed of a milling machine. The faces of the tetrahedron were fabricated until an edge length of 39.75 ± 0.13 mm was obtained by rotating the indexing head by 120° intervals and feeding the pyrophyllite into a vertical milling tool.

After the tetrahedron was removed from the steel rod, the following steps were taken to fabricate the test sample cavity:

1. Using Crystalbond 509, the tetrahedron was mounted on a 32 by 32 by 6.4-mm steel plate having a 12.7-mm diameter hole. The hole location as well as tetrahedral position (in dashed lines) is shown in Figure B-2.

2. The apex of the tetrahedron mounted on the steel plate was ground flat using a 600 grit diamond wheel. (This left a small triangular face on which the center could be pinpointed to start a pilot drill for step 3.)

3. A hole was drilled at the center of this triangle using a 0.18-mm diameter drill.

4. Using this hole as a pilot, a larger hole (its size depends on the number of electrical leads required) was drilled into the tetrahedron 9.53 mm deep. (Care was taken in drilling pyrophyllite; it appeared to be nonuniform in hardness and small drill bits were easily broken.)

5. The assembly was placed in a wafering machine (Figure B-3) and the apex tetrahedron was removed using a 15.2-cm diameter by 0.5-mm thick 600 grit diamond blade.

---

*Trademark, Aremco Products, Inc.

46HA922283-29

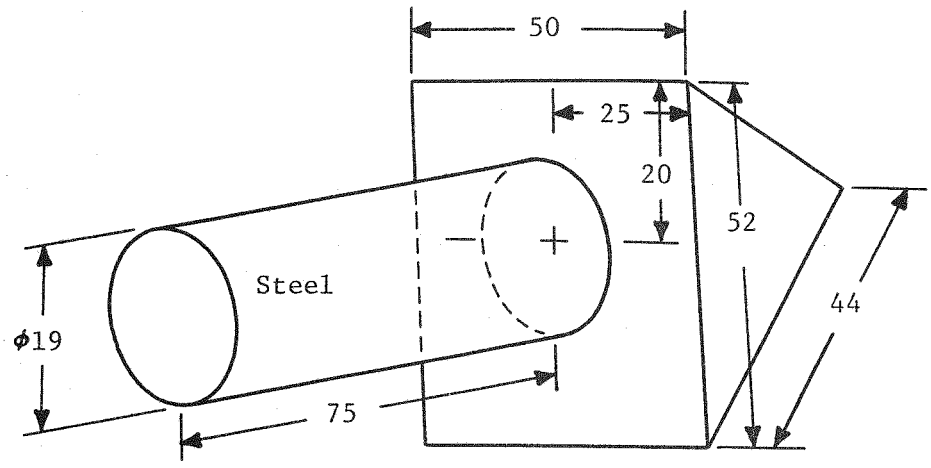

Figure B-1. Location of Steel Holding Rod on Pyrophyllite Prism. The attachment is made using a thermoplastic adhesive which melts at approximately 135°C. This assembly is positioned in a milling machine and the pyrophyllite is shaped into a tetrahedron. Dimensions in millimeters.

46HA922283-30

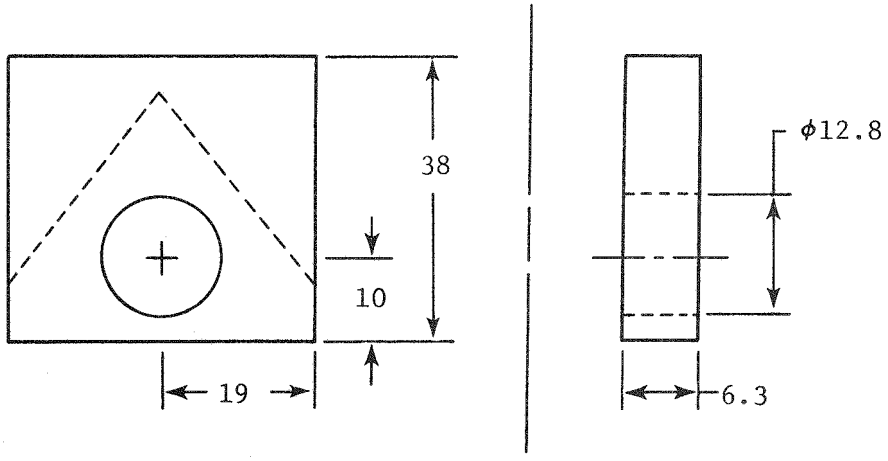

Figure B-2. Configuration of Steel Backup Plate Used to Hold Tetrahedron for Fabrication of Test Specimen Cavity. Dimensions in millimeters.

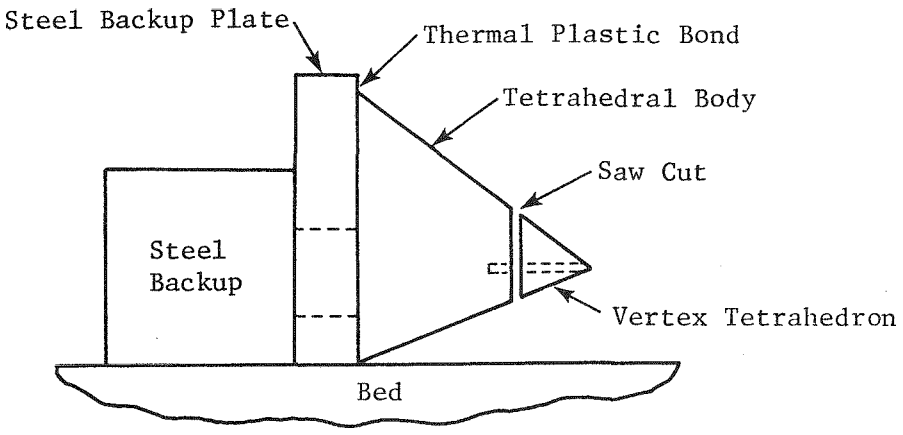

Figure B-3. Position of Tetrahedron Support Assembly on Bed of Wafering Machine

6. The apex tetrahedron was then hardened by heating to approximately 975°C and holding at the peak temperature for 20 minutes. The heat-up was approximately 8° C per minute. (This process, when performed in air, changed the color of pyrophyllite from grey to pink. When performed in an inert atmosphere, the color remained grey but the pyrophyllite appeared to have transformed to the same hardness.)

7. With the bulk of the tetrahedron still mounted on the steel plate, a 6.35-mm diameter hole was drilled through the tetrahedron using the center of the equilateral triangle left by the apex tetrahedron as the starting position. The truncated tetrahedron was removed from the steel plate.

8. Because of the 0.5-mm saw blade gap left when the apex tetrahedron was removed, it was necessary to fill this space with a 0.5-mm thick pyrophyllite spacer. A triangular shaped 0.5-mm thick slab was bonded to the truncated tetrahedron using an epoxy adhesive. The 6.35-mm diameter hole was extended through the shim and then reamed using a size "G" (6.477-mm diameter) drill. The edges of the shim were filed flush with the edges of the tetrahedron.

9. The apex tetrahedron and truncated tetrahedron were ultrasonically cleaned in acetone and then dried at 200°C. These parts were stored in a desiccated cabinet until ready to use.

APPENDIX C

CONSTRUCTION OF THE MANGANIN CELL

Manganin wire can be obtained with either enamel or cloth (silk or cotton) electrical insulation. Initially it was believed that the cloth insulation was preferable because of the possible loss in accuracy resulting from the structural support provided by enamel. However, when cloth-insulated Manganin wire was evaluated, it was found that the dielectric fluid media used became conductive in the high electric fields. This was apparently due to a transfer of contaminants from the cloth to the fluid. As a consequence, it was necessary to consider enameled Manganin wire.

The initial series of tests on enameled Manganin wire were run using 0.0355-mm diameter wire with a resistance of 3.94 ohms/cm.* Several test cells consisting of 25- to 30-cm lengths of this Manganin wire wound on plastic bobbins were fabricated and evaluated in the tetrahedral press. The resistance response of the Manganin wire with pressure was substantially out of line with the reported characteristics of Manganin wire.[60] On subsequent runs a larger size, 0.0799-mm diameter enameled Manganin wire, was used.** Details concerning the calibration of this wire are given in Appendix H.

The Manganin wire was wound on a polyethylene bobbin. Teflon*** was used initially but it has an inherent 0.54 GPa phase transition. The bobbin not only provided support for the wire but also provided an alignment and lead separation mechanism for the ferroelectric sample lead wires. A stereomicroscope was used as an aid throughout the assembly of the cell. The steps followed in the construction of the Manganin pressure cell are as follows:

1. A bobbin was fabricated to the dimensions shown in Figure C-1 from 6.35-mm diameter polyethylene rod.

2. A thin layer of Crystalbond 509 was placed on the mid-portion of the bobbin by heating the bobbin and Crystalbond 509 to 250°C and using a small diameter wire to spread and adjust to the correct amount.

---

*Manganin wire manufactured by W. B. Harris, Newark, N. J.
**Obtained from I. Fritz, Sandia Laboratories, Albuquerque, New Mexico
***Trademark, E. I. du Pont de Nemours & Co.

46HA922283-32

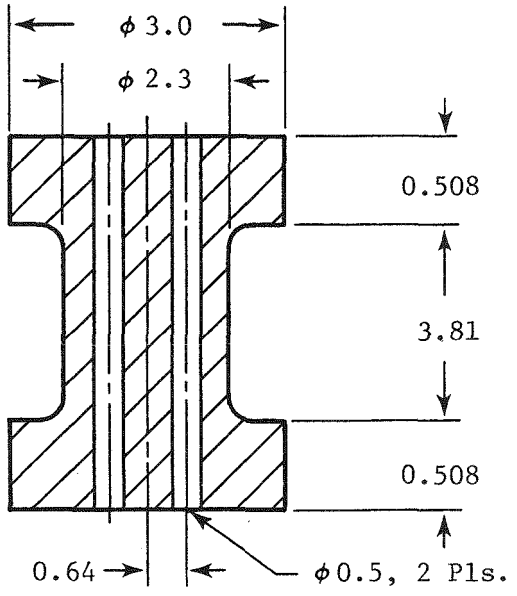

Figure C-1. Configuration of Polyethylene Bobbin Used to Support Manganin Wire. Two center holes are used to guide leads to the FE sample. Dimensions in millimeters.

3. A 3-cm length of wire (No. 28 magnet wire) was fed through the holes of the bobbin as shown in Figure C-2. The ends of the wire were clamped in the jaws of a pin vise.

4. Four 0.018-mm diameter holes were drilled into the bobbin as shown in Figure C-3.

5. A 35- to 40-cm length of Manganin wire was measured and one end was fed into two of the four holes (Figure C-4), leaving a 3-cm long leader.

46HA922283-33

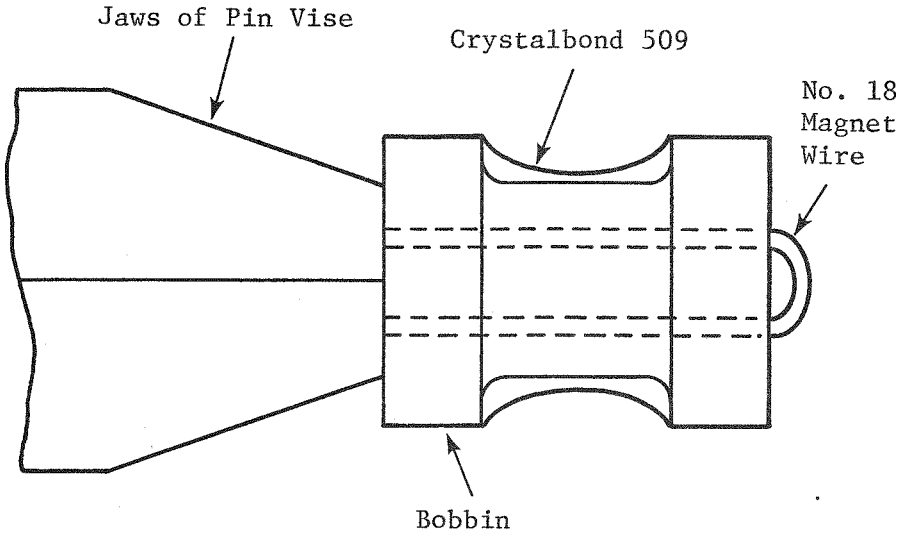

Figure C-2. Positioning of Bobbin in Pin Vise in Preparation for Winding Manganin Wire. Crystalbond 509 thermoplastic adhesive, which is later dissolved away, separates the Manganin from the bobbin so the wire is floating.

46HA922283-34

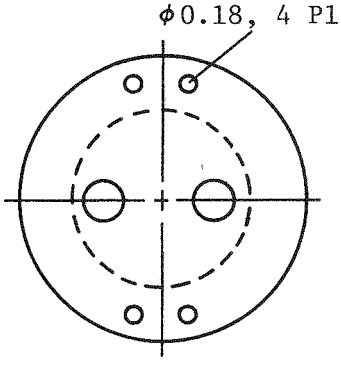

Figure C-3. Location of 0.18-mm Diameter Holes in Bobbin. The holes provide a mechanism by which the Manganin can be held to bobbin. Dimensions in millimeters.

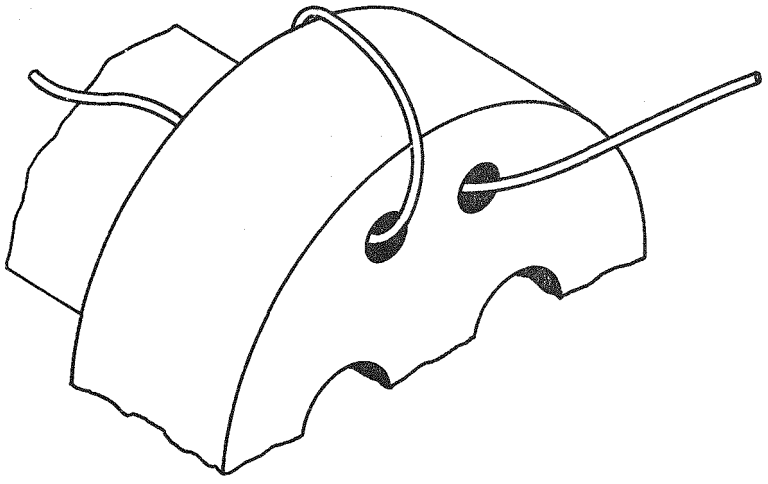

Figure C-4. Method of Holding Manganin Wire to Bobbin by Feeding Through Two 0.18-mm Diameter Holes

6. By placing the pin vise in a lathe and rotating it at a slow speed, the Manganin was uniformly wound on the bobbin. This was a manual operation in which the wire was kept taut by holding it in a thin-cotton-gloved hand. When completed, the free end was fed into the two remaining 0.018-mm diameter holes.

7. The cell was removed from the pin vise and the two leads of the Manganin wire were stripped of enamel to within 1 to 3 mm of the bobbin using Epoxystrip*. This required great care; tweezers and cotton swabs were used.

8. The magnet wire was removed and the cell was ultrasonically cleaned in acetone. During this cleaning, the Crystalbond 509 about the bobbin dissolved, allowing the coiled Manganin wire to remain suspended from the bobbin.

*Trademark, Beck Chemicals, Inc.

APPENDIX D

FERROELECTRIC SAMPLES

Atmospheric-fired ceramics having a density of approximately 7.6 g/cc were used for these studies. This material was manufactured* using the slip case process and was available in 1.2-mm thick rectangular slabs which were ground to a thickness of approximately 0.4 mm using a 600 grit diamond wheel. The ground slab was cleaned and both sides were electroded using the sputter deposition technique. This process consisted of cleaning in an ion beam and then depositing approximately 4 microns of chrome followed by 16 microns of gold. Rectangular test samples measuring approximately 1.5 by 3.5 mm were then fabricated using a wafering machine.

Gold lead wires approximately 1 cm long and 0.16 mm in diameter were thermal compression bonded to the electroded surface using a Hughes ball bonding device**. It was necessary to stagger the lead location so that the portion of the specimen directly under the joint could support the force of the ball bonding tip. Gold lead wires smaller in diameter could have been used; however, these electrical leads also provided structural support for the sample. After ultrasonic cleaning in acetone and vacuum drying, all the specimens were tested by running a hysteresis loop.

Due to the excessive amount of specimen breakage which occurred during the experiment, material from six different lots of ferroelectric ceramics was used.

---

*Gulton Industries, Inc.
**Hughes Aircraft Co.

APPENDIX E

FABRICATION OF CAPSULE, PLUGS AND LEAD WIRES

The capsule used to contain the specimen, Manganin cell and dielectric fluid was fabricated from 6.35-mm o.d. 304 stainless steel tubing having a wall thickness of 0.152 mm. After cutting to a length of 20.3 mm, the capsule was deburred with a 1.27-mm diameter aluminum oxide mounted pointed wheel grinder. It was possible to deburr and slightly taper the ends of the tubing using this grinder. A cross-sectional view of the resulting capsule is shown in Figure E-1.

Polyethylene plugs fabricated as shown in Figure E-2 were used to contain the fluid in the cell. Holes were drilled in the bottom plug in order to feed the electrical lead wires into the cell. Electrical feedthrough constituted one of the major obstacles in this program. Numerous configurations were attempted. Initially uninsulated wire was used in conjunction with the cell configuration shown in Figure 9. Studies were performed in which leads were brought out through the tetrahedral vertex as well as through the pyrophyllite gaskets. In

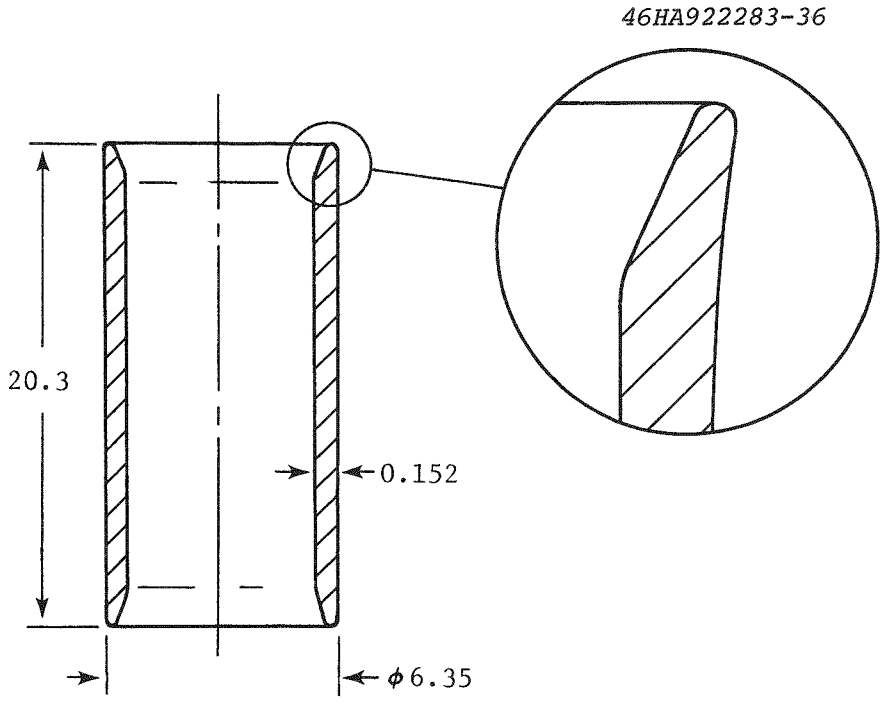

Figure E-1. Dimensions of 304 Stainless Steel Capsule Used to Contain Sample, Manganin Gage and Fluid. Dimensions in millimeters.

Figure E-2. Configuration of Polyethylene End Plug. Dimensions in millimeters.

most cases the lead wires not only frequently sheared off but when successful, it was not possible to perform electrical tests at high voltages. It was concluded that pyrophyllite becomes conductive in high electric fields. Finally two leads made of No. 28 magnet wire were found to be successful at high pressures and up to 2000 volts when tested in a cell similar to that shown in Figure 10.

It was necessary to feed six leads into the cell as follows: four for the two-terminal Manganin cell resistance measurement and two for the test specimen. One of the Manganin cell lead wires could have been connected to the specimen; however, the connection problems within the cell were more cumbersome than adding an additional lead.

Lead wire holes in the polyethylene were made by first manually drilling a pilot hole using a 0.18-mm diameter drill. Lead wire holes were then drilled through the polyethylene using a No. 80 drill (0.343-mm diameter). Threading the wire through this hole required stripping 7 to 10 cm of insulation from the end of the enameled magnet wire. The bare wire was then sanded to a taper over a 3- to 6-cm length (using 400 and 600 grit emery paper) and threaded through a hole. Once the end protruded, it was pulled through with needle-nose pliers. If care was taken, the same wire could be used for several holes.

The hole configuration on both the top and lower side of the bottom plug is shown in Figure E-3. Drilling these holes was achieved by resting a fixture containing the plug on an inclined plane at the appropriate angle to give the desired pattern. The pattern shown in Figure E-3 provided for lead wire separation within the cell and compaction of the lead wires at the point where they protruded and entered the vertex tetrahedron. The disadvantage of this configuration was that the Manganin cell and sample were not centered in the cell. Perhaps a more desirable configuration is illustrated in Figure E-4.

The length of the lead wire protruding from the lower surface of the bottom plug was approximately 15 cm. A sketch of the completed bottom plug assembly is shown in Figure E-5. The current and potential leads going to each side of the Manganin cell are continuous, making it possible to strip a small portion of the insulation from the wires using a pencil blasting* unit (SiO_2 abrasive was used). A small amount of 65-35 Pb-Sn soft solder then was placed on this uninsulated area.

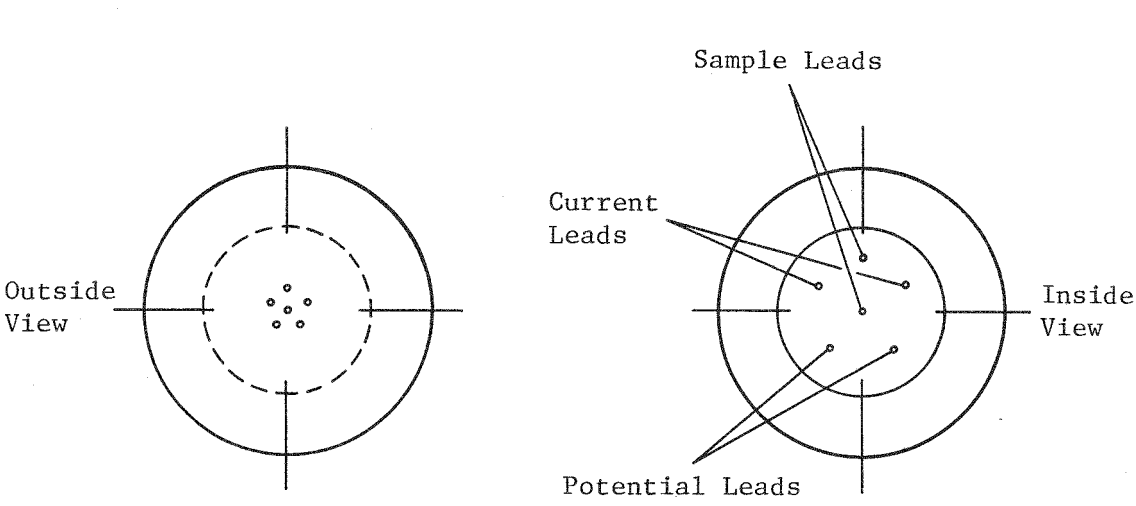

Figure E-3. Location of Lead Wire Holes in End Plug as Viewed from the End on the Outside of the Capsule and the End on the Inside of the Capsule

*Model F, S. S. White Co.

46HA922283-39

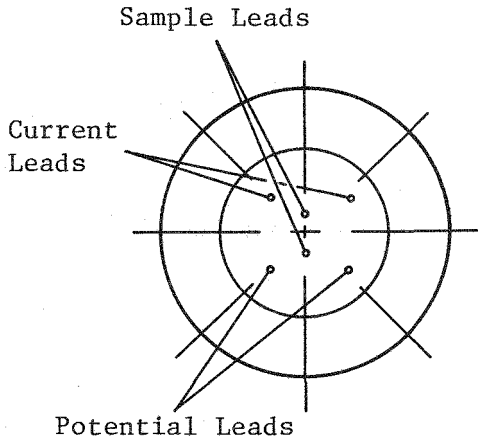

Figure E-4. A Possible Preferred Lead Wire Location in End Plug Which Has the Advantage That the Sample Lead Wires are Positioned Symmetrically on the Plug

46HA922283-40

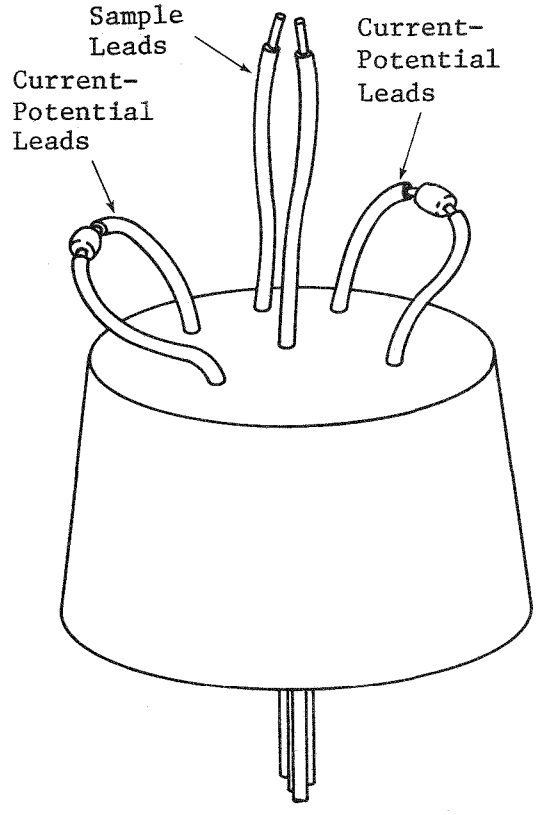

Figure E-5. The Final Configuration of the Polyethylene Bottom End Plug With Lead Wires in Place. The current-potential wires for four terminal resistance measurements are not separate but are used as an integral feedthrough.

APPENDIX F

DIELECTRIC TEST FLUID

Because most fluids solidify above 2 GPa,[61] and only a limited number are available as high pressure test media, Piermarini et al[62] have examined the fluidity of several liquids and found that a 4-to-1 mixture by volume of ethanol and methanol remained fluid to 10 GPa while a 1-to-1 mixture by volume of pentane and isopentane was fluid to at least 7 GPa.

Both fluid mixtures were examined; however, the alcohol mixture became conductive (apparently due to moisture pickup). Thus, pentane grade 1501* and isopentane grade 2370* mixture was the test fluid selected for use. Because of their excellent dielectric properties, it would have been desirable to use fluorocarbon liquids; however, fluidity data with pressure were not found.

During the initial phases of the program in which a variety of problems were encountered, extreme care was taken to ensure against moisture contamination, i.e., assembly of the test cell was performed in a dry room having a moisture content of less than 16 ppm or in a dry box. However, as the program progressed, it was found that these precautions were not necessary and it was possible to assemble and add fluid in the 50 to 60 percent humidity test site environment.

---

*Trademark, Fisher Scientific Co.

APPENDIX G

ASSEMBLY OF CAPSULE AND TEST CELL

The Manganin cell and test specimen were mounted in the capsule by soft soldering their leads to the magnet wire leads protruding through the bottom polyethylene plug. The recommended method of joining Manganin wire is by hard soldering.[63] This technique was attempted for the Manganin wire used in these studies, but difficulties were encountered because of the small sizes involved. Resistance welding was also attempted and was partially successful, but the weld tabs occupied an excessive amount of space in the capsule. Soft soldering appeared to be the only alternative. By using an ammonium chloride base flux and by wrapping the copper magnet wire several times with the Manganin wire, contact resistance was minimized.

The procedure used for test cell assembly was as follows:

1. The solder nodule deposited on the current-potential lead was flattened with smooth-faced pliers and a 0.71-mm diameter hole was manually drilled through the flattened region.

2. The Manganin cell was positioned on the end plug by feeding the two specimen lead wires through the holes provided. The Manganin leads were wound around each of the current-potential leads by threading through the 0.71-mm diameter hole and wrapping three to four times as shown in Figure G-1.

3. The solder was reflowed. A drop of ammonium chloride solder flux was used to aid in wetting the Manganin wire. The excess Manganin wire lead was cut off.

4. After ultrasonic cleaning in Freon TF* and acetone, the current-potential leads were drawn tight against the polyethylene plug.

5. The enamel insulation was removed from magnet wire sample leads. The uninsulated portions of the leads were cut to 3 to 5 mm in length and tinned with an 80% In-20% Pb solder using an ammonium chloride base flux. Gold lead wires, such as those ball-bonded to the ferroelectric test specimen, are less susceptible to embrittlement with indium-based (rather than tin-based) solders.

---

*Trademark, E. I. du Pont de Nemours & Co.

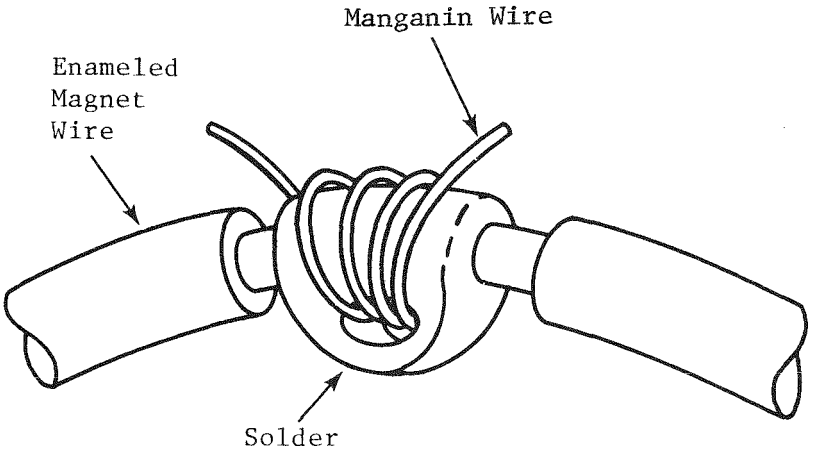

Figure G-1. Attachment of Manganin Wire to Current-Potential Lead Wire. After positioning the Manganin wire in place, the solder was reflowed.

6. The leads on the test specimen were cut to a length of 5 to 7 mm and attached to the plug lead wires by reflowing the In-Pb solder.

7. The assembly was ultrasonically cleaned in Freon TF, ethanol and acetone. After vacuum oven drying, the lead wires were drawn through a plug to reduce slack and position the test sample.

8. The lower plug was placed in the capsule. This was accomplished with an arbor press as shown in Figure G-2.

9. The capsule was filled with the dielectric fluid and the top plug was inserted using a technique similar to that shown in Figure G-2. The end plugs were flush with the ends of the capsule.

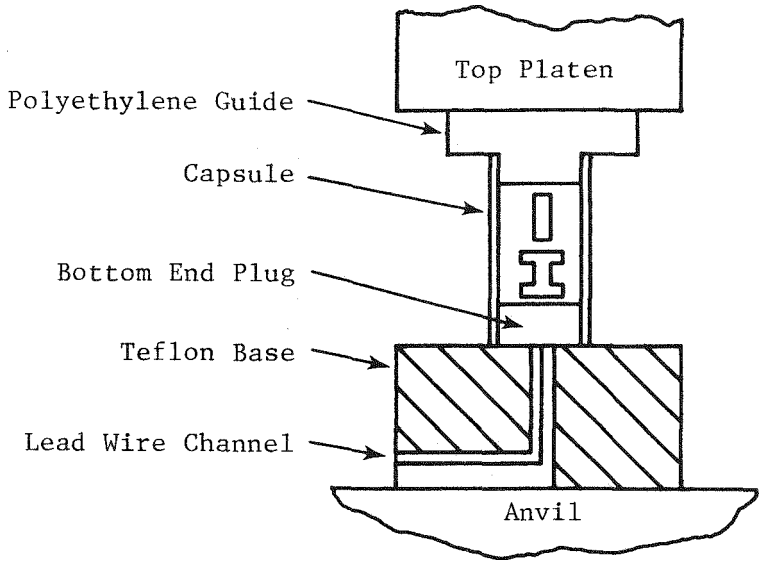

Figure G-2. Technique Used to Install End Plug in Capsule. After positioning the assembly in an arbor press, the end ap was forced into place.

10. The capsule was placed in the pyrophyllite tetrahedron and the lead wires were fed through the hole in the vertex tetrahedron. A room temperature curing epoxy adhesive was applied to the mating surfaces. The adhesive was polymerized under pressure by curing while mounted in an arbor press.

11. The electrical leads extruding from the assembly were cut into 15-cm lengths and the ends stripped of enamel and tinned. A 12-cm length of small diameter shrinkable tubing was slipped over the leads and drawn tight against the tetrahedron. Lengths of No. 20 Teflon insulated stranded copper electrical wire 1.5 cm long were soft soldered to the Manganin gage leads from the tetrahedron. The center lead of two 1.5-m long coaxial cables (RG174) were soldered to the ferroelectric sample leads. The free end of these leads had BNC connectors for attachment to the high voltage power supply and the capacitance bridge. Shrink tubing was used about each of the six connections.

APPENDIX H

CALIBRATION OF THE MANGANIN GAGE AND HEISE GAGE

At pressures up to 1.0 GPa, the resistivity of Manganin wire varies almost linearly with pressure although at higher pressures nonlinear effects are encountered. Decker et al[64] have examined the first-, second- and third-order fit of the pressure-resistance relationship and concluded that the second-order equation was the most representative. Their recommended relationship[65] which was based on the Hg_{S-L} (at 20.36°C) and Bi_{I-II} (at 23.5°C) transition is as follows:

$$p = 41.761\ (\Delta R/R) + 33.82\ (\Delta R/R)^2 \qquad (15)$$

where p is pressure in GPa.

Calibration of the Manganin wire used for this study was performed by examining its response in a gas (dry nitrogen) isostatic press as well as its response at the Bi_{I-II} transition using the tetrahedral press. For the gas isostatic press, calibration was performed using a BLH 100,000 psi (0.6895 GPa) pressure transducer which was accurate to ± 0.15 percent. This transducer is calibrated on a regular basis using a dead weight procedure. The same Manganin gage was used for all calibration tests. This gage as well as all others used in these tests was seasoned several times prior to use by heating to 140°C in a vacuum oven for 48 hours or more and then quenching in liquid nitrogen.

Four tests on the isostatic press were made for calibration purposes. These were performed slowly to reduce thermal effects. Approximately 20 data points were taken from zero to 0.68 GPa. The ambient temperature was approximately 23.5°C.

An uncertainty involved the zero pressure resistance reading which drifted slightly on both the isostatic press and the tetrahedral anvil device. Once pressure was applied, the readings stabilized. For the isostatic press, to obtain the zero pressure resistance value, a second-order fit of pressure versus resistance was determined. The result was extrapolated to zero and used to find $\Delta R/R$ for each of the four runs at a pressure of 0.6895 GPa with R calculated from the second-order fit of the data. The average value of $\Delta R/R$ was 0.01629.

The Bi_{I-II} transition pressure recommended for use by Decker et al[65] at 23.5°C is 2.5608 GPa. This value was originally reported by Heydemann[66] who examined the transition while the pressure was both increasing and decreasing. These values do not coincide; the hysteresis between them is called the region of indifference. The value selected was an average between the two.

The most common technique of obtaining fixed point calibration data measures resistivity changes of the material at the transition. However, based on a suggestion by A. A. Giardini[67] it was decided to make use of the Bi_{I-II} volume change at the transition. This was possible since $\Delta V/V$ was significant enough to affect the pressure within the test cell which could in turn be detected with the Manganin gage. The first successful test used a bismuth sample (grade B319*) weighing 0.19 g. A slight discontinuity in pressure at the Bi_{I-II} transition was observed. A sample weighing 0.427 g was used on the next two tests. The configuration of the calibration test cell is shown in Figure H-1. After each test, the cell was opened and the Bi sample examined. It was not distorted, indicating that the pressure environment about the bismuth was truly hydrostatic. Since the bismuth used was in granular form, a solid rod was made by melting a small amount in a 4-mm i.d. closed-end fused quartz tube. Although bismuth expands during solidification, the coefficient of expansion of bismuth is substantially greater than fused quartz and the sample usually fell out at ambient temperature.

For increasing pressure the results for test No. 3 (Figure H-2) show both the Bi_{I-II} transition as well as the 2.705 GPa Bi_{II-III} transition.[68] The magnitude of the Bi_{II-III} transition was surprising since the Bi_{II-III} resistance change noted in the open literature appears significantly smaller than the Bi_{I-II} transition.

For decreasing pressure the resistance change at the Bi_{I-II} transition is shown in Figure H-3. The region of indifference was approximately 0.1 GPa. For calibration purposes, an average $\Delta R/R$ based on the values at points A and B in Figure H-2 and H-3 were selected. As with data from the isostatic press, the zero resistance results were determined by fitting the gage resistance versus Heise gage reading to a second-order equation and extrapolating to zero. Pressure was applied at a slow rate to allow the temperature to reach equilibrium between each measurement.

---

*Trademark, Fisher Scientific Co.

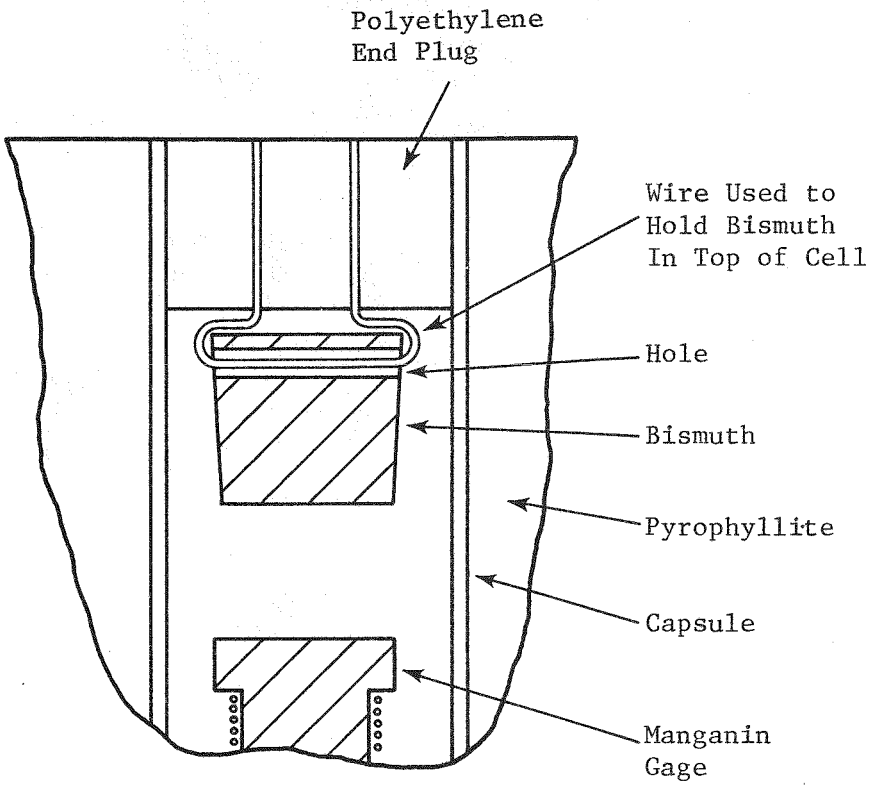

Figure H-1. Cross-section of Test Cell Configuration Used to Calibrate Manganin Gage Using Bismuth. The bismuth is tapered to allow the test cell to collapse and not interfere. The bismuth is held to the top end plug so that it will not contact the Manganin gage.

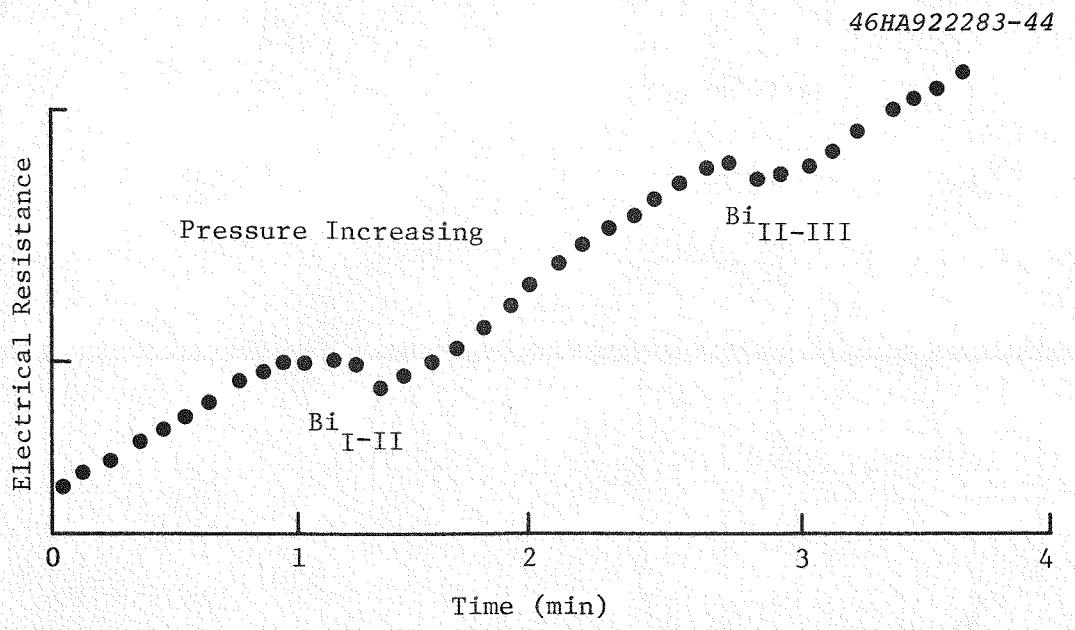

Figure H-2. Variation of Manganin Gage Electrical Resistance During Pressurization Cycle. At the transition a volume change results in a pressure change within the cell. A measurement was made approximately every 6 seconds.

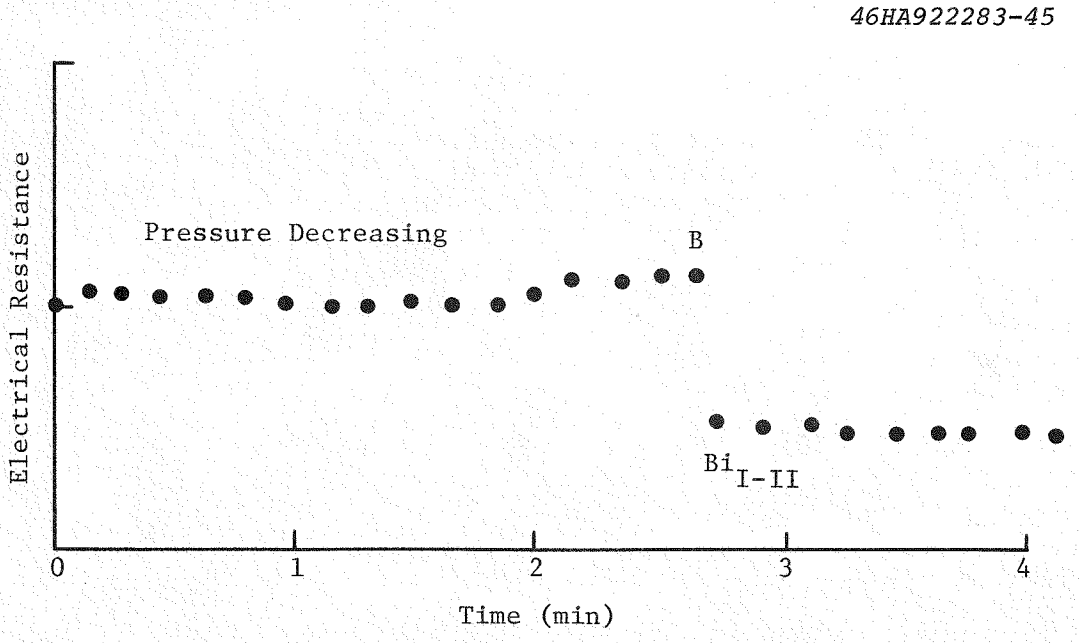

Figure H-3. Variation of Manganin Gage Electrical Resistance During Depressurization Cycle. The Bi_{I-II} phase change caused a change in pressure in the test cell because of its volume change. A measurement was made approximately every 11 seconds.

For the 2.5608 GPa Bi_{I-II} transition, $\Delta R/R$ was 0.057501. This, along with the isostatic press $\Delta R/R$ value of 0.01629 at 0.6895 GPa, resulted in the following calibration equation:

$$p = 41.623\ (\Delta R/R) + 43.892\ (\Delta R/R)^2 \qquad (16)$$

where p is pressure in GPa.

This equation agrees with Equation 15 within one percent up to the Bi_{I-II} transition. More detailed information concerning the Bi_{I-II} transition hysteresis is described by Zeto et al.[69]

While calibrating the Manganin gage it was also possible to determine the test cell pressure versus the Heise gage pressure reading on the tetrahedral anvil press control panel. This information was needed for the data reduction of a series of early tests in which defective Manganin wire was used. The accuracy of the calibration is questionable because the pressure transmitted to the sample is dependent on numerous factors such as the sample geometry and the rate at which pressure is applied. For instance, if pressure is applied rapidly, then higher pressures can be reached for a given Heise gage reading than at lower application rates. As mentioned previously, pressure was applied slowly for these tests. The resulting relationships are as follows:

for 0 to 1000 psi on the Heise gage,

$$p = 1.203 \times 10^{-3}\ (X) - 2.97 \times 10^{-7}\ (X)^2 \qquad (17)$$

and for 1000 to 5000 psi on the Heise gage,

$$p = 0.056 + 9.18 \times 10^{-4}\ (X) - 6.73 \times 10^{-8}\ (X)^2 \qquad (18)$$

where X is the Heise gage reading in psi and p is pressure in GPa.

ACKNOWLEDGMENTS

Thanks are extended to the following persons for their role in this project: Dr. E. K. Walsh, University of Florida, Gainesville, Florida, for his guidance and counsel; Dr. E. D. Whitney, University of Florida, for offering the tetrahedral anvil apparatus for use; Dr. A. A. Giardini, University of Georgia, Athens, Georgia, for demonstrating the operation of his tetrahedral anvil apparatus as well as for many other helpful suggestions; Dr. J. D. Barnett, Brigham Young University, Provo, Utah, for his suggestions on test sample configuration; Dr. A. A. Samara, Sandia Laboratories, Albuquerque, New Mexico, for his high pressure testing suggestions; and Dr. P. C. Lysne and Dr. C. M. Percival, Sandia Laboratories, Albuquerque, New Mexico, for their advice concerning shock depolarization dielectric requirements. The effort extended by Mr. J. R. Novak and Mr. F. H. McNabb of the General Electric Neutron Devices Maintenance Organization for their role in rebuilding the press is greatly appreciated. Thanks are extended to Mr. J. L. Pethe of the General Electric Company for his effort in constructing the low voltage looper.

REFERENCES

1. F. W. Nielson, Sandia Memo No. 230B-56-51 (Sandia Corp., Albuquerque, N. M., November 1956).

2. E. Sawaguchi, J. Phys. Soc. Japan 8, 615 (1953).

3. D. A. Berlincourt, Annual Progress Report on Piezoelectric Materials, Sandia Labs P. O. No. 51-6542 (Sandia Corp., Albuquerque, N. M., March 1960).

4. G. W. Anderson, Sandia Memo No. 224-57-51 (Sandia Corp., Albuquerque, N. M., August 1957).

5. P. C. Lysne and C. M. Percival, J. Appl. Phys. 46, 1519 (1975).

6. P. J. Chen and M. C. McCarthy, Int. J. Solids Structures 10, 1229 (1974).

7. P. C. Lysne, Private Communication.

8. V. V. Danial, Dielectric Relaxation (Academic Press, New York, 1967), p 91.

9. Reference 8, p 93.

10. C. B. Sawyer and C. H. Tower, Phy. Rev. 35, 269 (1930).

11. G. A. Samara, Phys. Rev. 151, 382 (1966).

12. Reference 3, p 48.

13. D. A. Berlincourt, IEEE Trans. Solids and Ultrasonics SU-15, 89 (1968).

14. C. Kittel, Phys. Rev. 82, 729 (1951).

15. B. Jaffe, Proc. IEEE, 61, 1264 (1961).

16. F. Jona and G. Shirane, Ferroelectric Crystals (Macmillan Co., New York, 1962), p 16.

17. Reference 16, p 26.

18. Reference 2, p 18.

19. H. M. Barnett, J. Appl. Phys. 33, 1606 (1962).

20. S. Roberts, J. Am. Ceram. Soc. 33, 66 (1950).

21. B. Jaffe, W. R. Cook, and H. Jaffe, Piezoelectric Ceramics (Academic Press, New York, 1971), p 123.

22. D. A. Berlincourt and H. H. A. Krueger, Annual Progress Report on Piezoelectric Materials, Sandia P. O. No. 51-9689-A (Sandia Corp., Albuquerque, N. M., April 1963), p 3.

23. Reference 2, p 624.

24. Reference 19, p 136.

25. R. H. Dungan, H. M. Barnett, and A. H. Stark, J. Am. Ceram. Soc. 45, 382 (1962).

26. M. Torccaz, L. Eyraud, Y. Fetiveau, P. Gonnard, and J. Paletto, CR Acad. Sciences Paris t 275, Serie B 597 (1972).

27. Reference 25, p 384.

28. Reference 25, p 385.

29. Reference 22, p 18.

30. Reference 22, p 22.

31. Reference 22, p 26.

32. Reference 26, p 597.

33. G. A. Samara, Advances in High Pressure Research, R. S. Bradley, Ed. (Academic Press, Inc., New York, 1969), p 172.

34. G. A. Samara, Ferroelectrics 2, 281 (1971).

35. G. A. Samara, Phys. Rev. 151, 378 (1966).

36. Reference 34, p 282.

37. Reference 11, p 380.

38. G. A. Samara and A. A. Giardini, Phys. Rev. 140, A954 (1965).

39. I. N. Polandov, V. I. Kalinin, N. P. Kachalov, and G. P. Isaev, Vestnik Moskovskogo Universitita, Khimiya, 30, 244 (1975).

40. Reference 22, p 110.

41. P. Gonnard, Y. Fetiveau, F. Bauer, and L. Eyraud, C. R. Acad. Sc. Paris t 275, Serie B 633 (1972).

42. W. J. Halpin, J. Appl. Phys. 37, 153 (1966).

43. C. E. Reynolds and G. E. Seay, J. Appl. Phys. 32, 1401 (1961).

44. C. E. Reynolds and G. E. Seay, J. Appl. Phys. 33, 2234 (1962).

45. D. G. Doran, F. E. Materials Under Shock, SR1 Project No. PGD-3483 (Stanford Res. Inst., Menlo Park, Calif., Nov. 1962).

46. D. G. Doran, J. Appl. Phys. 39, 40 (1968).

47. R. K. Linde, J. Appl. Phys. 38, 4839 (1967).

48. Reference 43, p 1402.

49. P. C. Lysne, R. A. Graham, L. C. Bartel, and G. A. Samara, "Shock Wave Induced Phase Transformation: A Review of the Field," Report No. SC-TM-710907 (Sandia Corp., Albuquerque, N. M., 1971).

50. Reference 46, p 46.

51. J. W. Nunziato and E. K. Walsh, Arch. Rational Mech. Anal. 64, 299 (1977).

52. M. A. Goodman and S. C. Cowin, Arch. Rational Mech. Anal. 44, 249 (1972).

53. H. T. Hall, Rev. of Sci. Inst. 29, 271 (1958).

54. E. C. Lloyd, U. O. Hutton, and D. P. Johnson, J. Res. N. B. S. C Eng. and Inst. 63C, 59 (1959).

55. Reference 53, p 272.

56. M. D. Banus and S. D. Nye, Rev. of Sci. Inst. 35, 1321 (1964).

57. H. T. Hall, Progress in Very High Pressure Research, F. P. Bundy, W. R. Hibbard, and H. M. Strong, Eds. (John Wiley and Sons, New York, 1961), p 4.

58. J. Lees, Nature 203, 967 (1964).

59. D. L. Decker, J. D. Jorgensen, and R. W. Young, High Temp. - High Press. 7, 332 (1975).

60. D. L. Decker, W. A. Bassett, L. Merrill, H. T. Hall, and J. D. Barnett, J. Phys. Chem. Ref. Data 1, 773 (1972).

61. P. W. Bridgman, Collected Experimental Papers (Harvard U. Press, Cambridge, Mass., 1964).

62. G. J. Piermarini, S. Block, and J. D. Barnett, J. Appl. Phys. 44, 5377 (1973).

63. S. E. Babb, Jr., High Pressure Measurements, A. A. Giardini and E. C. Lloyd, Eds. (Butterworths, Washington, 1963), p 124.

64. Reference 60, p 817.

65. Reference 60, p 820.

66. P. L. M. Heydemann, J. Basic Eng. 89, 551 (1967).

67. A. A. Giardini, Private Communication.

68. G. C. Kennedy and P. N. LaMari, Progress in Very High Pressure Research, F. P. Bundy, W. R. Hibbard, and H. M. Strong, Eds. (John Wiley and Sons, Inc., New York, 1961), p 304.

69. R. J. Zeto, H. B. Vanfleet, E. Hryckowian, and C. D. Bosco, N. B. S. Bull No. 326 (N. B. S., Washington, D. C., 1968).